Ripply1 and Gsc collectively suppress anterior endoderm differentiation from prechordal plate progenitors

Tao Cheng[1,2#], Xiang Liu[2#], Yang Dong[1,2#], Yi-Meng Tian[2], Yan-Yi Xing[1,2], Chen-Yi Chen[2], Cong Liu[2], Yun-Fei Li[2], Ying Huang[2], Ding-Hao Zhuo[2], Xiao Xu[1], Jing-Yun Luan[2], Xin-Xin Fu[2], Zi-Xin Jin[2], Jing Mo[3], Xiang Xu[2], Hong-Qing Liang[1,2]*, Peng-Fei Xu[1,2]*

[1] Women's Hospital, Zhejiang University School of Medicine, Hangzhou, China.

[2] Institute of Genetics and Department of Human Genetics, Zhejiang University School of Medicine, Hangzhou, China.

[3] Department of Immunology, Guizhou Medical University, Guiyang 550004, China.

*Corresponding author: lianghongqing@zju.edu.cn, pengfei_xu@zju.edu.cn

[#]Tao Cheng, Xiang Liu and Yang Dong contributed equally to this work and should be regarded as joint first authors.

Abstract:

During gastrulation, the mesendoderm is firstly specified by morphogens such as Nodal, and then segregates into endoderm and mesoderm in a Nodal concentration-dependent manner. However, the mechanism underlying the segregation and crosstalk of different sub-groups within the meso- and endoderm lineages remains unclear. Here, taking zebrafish prechordal plate (PP) and anterior endoderm (Endo) as research model, using single-cell multi-omics and live imaging analyses, we show that anterior Endo progenitors originate directly from PP progenitors. A single-cell transcriptomic trajectory analysis of wild-type, *ndr1* knockdown and *lft1* knockout Nodal explants confirms the diversification of anterior Endo fate from PP progenitors. Gene Ontology (GO) enrichment analysis indentifies that the change of chromatin organization potentiates the segregation of endodermal cell fate from PP progenitors. Single-cell ATAC & RNA sequencing further reveals that two transcriptional regulators, *gsc* and *ripply1*, exhibit varied activation patterns in PP and Endo lineages at both the chromatin and RNA expression levels. We further demonstrate that Ripply1 functions coordinately with Gsc to repress endodermal cell fate by directly binding to the *cis*-elements of *sox32* and *sox17*. Modulating the expression levels of these regulators tilts the cell fate decision between the PP and Endo lineages.

Introduction:

During gastrulation, instructed by genetic and epigenetic signals, naïve cells from blastula progressively acquire distinct cell fates and are allocated to specific domains within the embryo[1,2]. Nodal, a member of the transforming growth factor β (TGF-β) superfamily, acts as a morphogen[1,3-5] and plays highly conserved roles in mesendoderm induction and patterning[6-8].

It is widely accepted that Nodal induces endodermal and mesodermal cell fates via its concentration gradient[8-10]. Higher Nodal signaling activity bias cells toward endoderm, while lower levels are thought to promote mesoderm induction[11,12]. Mesodermal and endodermal common progenitors are induced by Nodal and mixed together at the onset of gastrulation[1], while it remains elusive how the common progenitors of mesendoderm took on distinct lineages. Several recent studies reported that multiple important signaling pathways interacted with

Nodal to drive mesendoderm separation[2,13-15]. Notably, lateral endoderm specification may comply with a stochastic cell fate switching model in zebrafish[16].

The specification of dorsal mesendoderm requires the highest level of Nodal signaling, as evidenced by that this cell population was first to be depleted when Nodal signaling was gradually inhibited[11]. Both the PP and anterior Endo originate from anterior mesendoderm (derived from the dorsal mesendoderm), and the commitment of these cell fates is regulated by similar levels of Nodal signaling. However, the mechanisms governing the separation of cell fates within the anterior mesendoderm remain unclear. Previous studies show that Nodal signaling enhances the duration of cell-cell contact in PP cells, creating a positive feedback loop between cell-cell contact duration and cell fate specification[17]. However, what factors downstream of Nodal pathway play major roles in segregating these two cell fates, when and how PP and Endo cells can be distinguished transcriptionally are the questions remaining to be investigated.

Previous research has shown that Gsc, whose expression can be induced by Nodal, acts as a repressor to suppress anterior endoderm specification by binding to the promoter region of *sox17*[18]. However, investigations into loss-of-function of Gsc in zebrafish have not yielded conclusive evidence supporting its significant roles in mesoderm and/or endoderm specification[19,20]. These results imply that there might be additional, unidentified transcriptional repressors that work in collaboration with Gsc and possess a redundant function in suppressing the specification of endoderm.

In this study, we constructed a single-cell transcriptional trajectory to delineate the cell state segregation between PP and anterior Endo in zebrafish embryos and Nodal-injected zebrafish explants[21,22]. Single-cell transcriptional trajectory and live imaging analyses demonstrated that anterior Endo cells originated and were specified from PP progenitors. Interestingly, this lineage separation can be traced back to as early as the onset of gastrulation. To achieve a more comprehensive understanding, we integrated single-cell datasets from wild-type, *ndr1* (Nodal ligand) knockdown and *lft1* (Nodal inhibitor) knockout Nodal explants at shield stage to construct an extended single-cell trajectory, which fully captured the branching event between PP and anterior Endo fates and unveiled a potential involvement of epigenetic

regulation in this process. This finding was further supported by the experimental evidence that perturbation of the chromatin remodeler *srcap* could affect the cell specification of PP and anterior Endo. Furthermore, combining the multi-omic analysis and gain-/loss-of-function experiments, we found that a transcriptional repressor, Ripply1, cooperated with Gsc to supresse endoderm specification by directly binding to the regulatory elements of *sox17* and *sox32*.

Results:

Anterior Endo originates from PP progenitors in zebrafish.

Both anterior Endo and PP are derived from embryonic shield and require high Nodal signaling to be specified[11,18,23]. To investigate how these two cell lineages are further segregated, we collected the single-cell RNA-seq datasets from the published studies[24,25], identified the subpopulations representing the anterior Endo and PP cells, and reconstructed their lineage branching tree (Figures 1A-1C and S1A). We found that these two lineages started to be separated at shield stage, and their common progenitors highly expressed PP marker genes, like *gsc, frzb*, etc. (Figures 1C and S1A). Then, we further explored the dynamic molecular signatures of these two lineages during their fate determination. Pseudotime analysis revealed that PP and Endo exhibited distinct differentiation states by the end of gastrulation (Figure S1B). Of note, compared to *sox32*, *gsc* displayed earlier transcriptional differences in these two lineages (Figure S1C). The Uniform Manifold Approximation and Projection (UMAP) analysis[26] and PCA analysis showed that the common progenitors of PP and Endo clustered closely to PP and away from Endo (Figures S1D and S1E), suggesting that anterior Endo lineage is branched out from PP lineage. The cell lineage prediction analysis[27] also revealed that the progenitor cells resembled more of the PP lineage (Figures 1D, 1E and S1F), and similar result was obtained using another single-cell RNA-seq dataset (Figures S1G-S1I). Therefore, both UMAP and the cell lineage prediction analysis suggest that anterior Endo and PP originate from the same progenitor with transcriptome profile more similar to PP lineage. Anterior Endo becomes transcriptionally distinguishable from PP as early as at the shield stage.

Cells from hatching gland (derived from PP) and pharyngeal pouch (derived from anterior

Endo) are distant on the transcriptome-based phylogenetic tree of zebrafish embryos[25]. Thus, the resolution of this dataset may not be sufficient to identify the exact lineage separation point between PP and Endo. To investigate the key molecules that regulate the PP and Endo separation, we employed our previously published Nodal induced embryonic explant system (referred to Nodal explant hereafter), which encompasses the axial mesendoderm, along with the PP and anterior Endo lineages[22]. Notably, the single-cell trajectory tree of Nodal explants showed a closer transcriptomic relationship between the PP and anterior Endo (Figure 1F). Thus, we reconciled the single-cell transcriptome dynamics to look for the branching point of PP and anterior Endo in the Nodal explants (Figures 1G, 1H, S2A and S2B). Consistent with the observations in wild-type embryos, the common progenitors of these two lineages highly expressed the PP marker gene (*gsc*), and the segregation between PP and Endo had already occurred by 6 hpf (hours post fertilization) (Figures 1G, 1H and S2B). Cell lineage prediction analysis on the Nodal explant datasets further indicated that the common progenitor cells were transcriptionally similar to PP (Figures 1I and S2I), which aligned with our previous observations in wild-type embryos (Figures 1D, 1E, S1H and S1I).

To explore the molecular signatures during the specification of PP and anterior Endo, we performed differential expression analysis for these two lineages in both wild-type embryos and Nodal explants. 18 genes were highly enriched along the trajectory of Endo specification in both wild-type embryos and Nodal explants (Figure S2C). These genes enriched GO terms such as “gland development”, “negative regulation of transcription, DNA-templated” and “negative regulation of RNA biosynthetic process” (Figure S2D). While for PP, 49 highly expressed genes were identified (Figure S2C), which enriched GO terms including “proteolysis involved in cellular protein catabolic process”, “cellular protein catabolic process” , “protein catabolic process”, etc. (Figure S2D). Cell fate specification requires the activation of a series of genes, and these gene sets can be regarded as gene modules, which are probably responsible for specific lineage formation[28]. We identified two gene modules associated with Endo and PP lineages respectively (Figure S2E). Gene Ontology enrichment analyses[29] showed that terms like “endoderm development” and “cell motility” were enriched for Endo (gene module 1), while “embryo development ending in birth or egg hatching” was enriched for PP (gene module

2) (Figures S2F-S2H). These enriched GO terms were highly correlated with the developmental processes and functions of these two cell types.

To further validate this observation and investigate the dynamics of lineage segregation between anterior Endo and PP during development, we performed live imaging analysis on embryos of Tg(*gsc*:EGFP;*sox17*:DsRed) (Figures 2A and 2B). Notably, we observed a gradual emergence of *sox17*-positive cells from a subset of the *gsc*-positive cells (Figures 2A-2D, S3A-S3D and Movies S2, S3). And this cell fate transition was also evident in Nodal explants constructed from Tg(*gsc*:EGFP;*sox17*:DsRed) embryos (Figures S3E-S3H and Movie S1). Furthermore, we generated *sox17*:Cre and *gsc*:loxP-STOP-loxP-mCherry constructs (Figure S4D) and co-injected them with transposase mRNA into one-cell stage embryos (Figure S4A). Interestingly, distinct mCherry-positive cells were observed in the injected embryos, providing clear evidence that *gsc*-positive cells can give rise to *sox17*-positive cells (Figures S4B and S4C).

We co-stained *gsc* and *sox17* in embryos and in Nodal explants respectively at different time points during gastrulation (Figures 2E and S3I). By assessing the expression levels of *sox17* and *gsc* in *sox17*-positive anterior mesendoderm cells, we observed a positive correlation between *sox17* and *gsc* expression at the onset of gastrulation. However, with advancing development, *sox17* and *gsc* expression exhibited a negative correaltion in both embryos and Nodal explants (Figures 2F and S3J). This suggests that the increase of *sox17* expression during anterior Endo differentiation is accompanied by the simultaneous reduction of *gsc* expression. These findings align with our live imaging experiments (Figures 2A, S3B and S3F). In summary, combing single-cell tanscriptomic trajectory analyses and live imaging experiments using embryos and explants, we demonstrated that anterior Endo cells were derived from PP progenitor cells in zebrafish.

Nodal-Lefty regulatory loop is needed for PP and anterior Endo fate specification

In zebrafish, the PP and anterior Endo lineages are physically in close proximity and direct contact[17]. During development, interactions through cell-cell contacts between neighboring cell types often play a crucial role in promoting cell fate segregation[17,30]. We hypothesized that

174 communications between PP and anterior Endo cells may influence each other's cell fate
175 specification. We employed LIANA[31], a ligand-receptor analysis framework, to investigate the
176 molecular signals involved in these interactions using single-cell RNA-seq datasets. Our
177 analysis revealed strong interactions between PP and Endo cells in both wild-type embryos and
178 Nodal explants (Figures S5C-S5F). Interestingly, key molecular factors in the Nodal-Lefty
179 regulatory loops (Figure 3D), such as *ndr1*, *lft1* and *lft2*, were significantly enriched when
180 setting PP as source cells and Endo as target cells (Figures 3A, S5A, S5B and S5G-S5I), while
181 Nodal-Lefty interactions were reduced when setting the cell types conversely (Figures 3B and
182 S5G-S5I). In addition to Nodal-Lefty signaling, Fgf and Wnt signalings were also significantly
183 enriched in cell-cell communications between these two cell types in both embryos and Nodal
184 explants (Figures 3A, 3B and S5G-S5I). This observation is consistent with previous findings
185 that Fgf signaling interacts with Nodal to regulate mesoderm and endoderm separation[13,32].

186 The results presented above suggest that differences in the Nodal-Lefty signaling may exist
187 between PP and anterior Endo cells. It is widely accepted that Nodal-Lefty functions as
188 reaction-diffusion system to facilitate Nodal gradient formation and cell fate determination[33-37]
189 (Figure 3D). As zebrafish possess redundant Nodal (Ndr1, Ndr2 and Ndr3) and Lefty (Lefty1
190 and Lefty2) paralogs, we firstly investigated the perturbation effects of individual Nodal or
191 Lefty paralog on Nodal activity and its gradient. We generated an ectopic Nodal gradient in
192 zebrafish animal pole cells by injection of *ndr2* mRNA at 128-cell stage in wild-type embryos,
193 *ndr1* morphants and *lft1* mutants (Figures 3E, S6A-S6F and S6H-S6M). By immunostaining
194 and quantification of the pSmad2 signaling, we observed a significant enhancement of Nodal
195 activity in *lft1* mutants, while its level decreased upon *ndr1* knockdown (Figures 3E, 3F and
196 S6A-S6M).

197 To further determine how Nodal-Lefty is involved in the regulation of PP and anterior
198 Endo separation, we performed single-cell transcriptomic sequencing for Nodal explants
199 constructed from *ndr1* morphants and *lft1* mutants at shield stage (Figure 3G). We integrated
200 these two single-cell RNA-seq datasets with the dataset of wild-type Nodal explants[22]. After
201 applying unsupervised clustering, we identified a total of 9 different cell clusters (Figures 3H,
202 S7A and S7B). Among these clusters, two mesodermal clusters named mesoderm_PP and

203 mesoderm_NT (Figure 3H) were obtained. Mesoderm_PP cells transcriptionally resembled the
204 progenitors of PP evidenced by the high expression of *gsc* and *chrd*, while mesoderm_NT cells
205 were the progenitors of notochord characterized by the high expression of *noto* and *tbxta*
206 (Figures S7A and S7B). We observed that a small cluster of *sox32* and *sox17* positive anterior
207 Endo cells was close to the PP cells on the UMAP (Figure 3H), further supporting the
208 transcriptional similarity between anterior Endo and the PP lineage. We then calculated the
209 proportions of PP and Endo cells in the three datasets, and found that the proportions of both
210 cell types increased in *lft1*-mutant explants, while decreased in *ndr1*-morphant explants
211 compared to wild-type explants (Figures 3I and S7C).

212 To better estimate Nodal activity during PP and Endo cell fate segregation, we defined a
213 Nodal score by regressing out the expression level of all the Nodal downstream targets, which
214 were differentially expressed upon Nodal treatment[22] and also possessed pSmad2 binding peaks
215 near their genetic loci[22,38] (**see Methods**). A total of 29 Nodal downstream targets, whose
216 expression exhibited a high correlation with Nodal activity, were used to calculate Nodal score
217 (Figure 3J). We found Nodal score was dramatically decreased in *ndr1* knockdown samples and
218 slightly increased in *lft1* mutant samples compared to that in wild-type samples (Figures 3K
219 and S7D), which is consistent with the results of pSmad2 immunostaining (Figures 3E and 3F).
220 We then examined the levels of Nodal score across all cell types in Nodal explants at 6 hpf, and
221 found that axial mesendodermal cells, including PP, notochord and anterior Endo, displayed the
222 highest Nodal scores (Figure S7E), which was consistent with previous knowledge that Nodal
223 activity was the highest in the dorsal margin of zebrafish embryos at the onset of
224 gastrulation[1,39,40]. A further comparsion of Nodel scores between PP and Endo revealed that PP
225 had a sightly higher Nodal score than Endo (Figure S7E). These analyses underscored the
226 importance of Nodal signaling levels in PP and anterior Endo lineage specification.

227

228 **A meticulous single-cell trajectory tree reveals the role of chromatin remodeling in PP and**
229 **anterior Endo segregation.**

230 To thoroughly investigate the dynamic transcriptome changes during PP and anterior Endo
231 separation, we reconstructed a single-cell trajectory tree using all PP and anterior Endo cells

232 from three Nodal explant datasets at 6 hpf which was a crucial time point previously identified
233 for the separation of these two lineages (Figure 4A). This trajectory tree captured a continuous
234 cell-state-transition process from PP progenitors to anterior Endo, and a key branching point in
235 this process was identified (Figures 4A and S7F). To elucidate the molecular dynamics in this
236 branching process, we performed differential expression analysis for these two lineages around
237 the branching point (Figure 4B). Three clusters of genes were identified, which were highly
238 expressed in pre-branch (progenitors), left-branch (Endo) and right-branch (PP) respectively.
239 GO enrichment analysis using these three gene sets identified terms related to mesendodermal
240 cell fate specification (Figure 4B). For instance, "regulation of endodermal cell fate
241 specification" was observed in Endo lineage, while "negative regulation of transcription by
242 RNA polymerase II" was found in PP lineage. Interestingly, "chromatin organization" was
243 significantly enriched in the pre-branch cells, and maintained high enrichment during PP
244 specification, but was down-regulated upon endodermal lineage formation (Figure 4B).
245 Furthermore, the GO term "chromatin organization" was also enriched in the differentially
246 expressed genes of the PP cells when comparing *lft1* mutant or *ndr1* knockdown samples to
247 wild-type samples (Figures 4C-4G and S7G).

248 These analyses unveiled a potential role of chromatin regulators in the regulation of PP
249 and anterior Endo segregation, prompting us to identify the specific factors involved in this
250 process. Among the candidates within GO term of "chromatin organization" (Figure 4B-4E),
251 we identified a key member of SWI/SNF complex, *srcap*, which was differentially expressed
252 between PP and Endo cells in both embryos and Nodal explants (Figures 4J, 4K and S7H).
253 Previous studies have demonstrated that the SWI/SNF nucleosome remodeling complex is
254 necessary for TGF-β-induced transcription of numerous target genes[41,42]. To investigate the role
255 of the SWI/SNF complex in the separation of PP and Endo cell fates , we treated embryos with
256 AU15330 (Figure 4H), a known degrader of SWI/SNF ATPase components[43]. Subsequently,
257 we assessed the cell fate specification of PP and anterior Endo lineages by HCR co-staining for
258 *gsc*, *frzb* and *sox32*. We found that the numbers of anterior Endo cells were significantly
259 increased in the embryos treated with AU15330 compared to DMSO-treated embryos (Figures
260 4H and 4I). Similar effects were observed in *srcap* morphants, where the cell number of anterior

Endo increased compared to wild-type embryos (Figures 4L, 4M, and S7I).

Collectively, these findings underscore the importance of SWI/SNF complexes in ensuring accurate cell fate segregation within the anterior mesendoderm.

Integrative analysis of single-nucleus RNA-Seq and ATAC-Seq reveals distinct chromatin states underlying differential expression profiling in PP and Endo cells.

To delve deeper into the involvement of chromatin states in the separation of PP and Endo, we conducted single-cell assays for transposase-accessible chromatin (ATAC) and nuclear RNA sequencing in zebrafish embryos at 6 hpf (Figure 5A). Recognizing that accurate cell clustering cannot solely rely on chromatin accessibility dataset, we integrated this dataset with RNA expression data to achieve precise cell type identification. The resulting cells were clustered into 10 different groups on the UMAP (Figures 5B, S8A, and S8B). Consistent with the earlier single-cell RNA atlas of Nodal explants, Endo was found to locate closely to the axis mesoderm (PP and notochord progenitors) on the joint UMAP (Figure 5B).

Using the marker gene *gsc*, we identified PP progenitor cells within the axis mesoderm, and then Endo and PP progenitor cells were selected for downstream analysis (Figure 5C). A small cluster of cells expressing *sox32*, *sox17* and *foxj1a*, which were located distantly from PP and Endo, were classified as dorsal forerunner cells (DFCs) and excluded from further analysis (Figures 5C and S8C).

Our data unveiled differential chromatin accessibility between PP and Endo cells (Figures 5G, S8K, and S8L). Correlation analysis revealed a strong correspondence between chromatin accessibility and RNA expression levels for marker genes in these two cell types (Figure S8D). To identify master regulators of PP and Endo separation, we performed differential analysis for both chromatin accessibility and gene expression (Figures 5D and S8E). A total of 170 up-regulated genes in PP, including *gsc* and *ripply1*, and 261 up-regulated genes in Endo, such as *sox32* and *sox17*, were identified. Most of these genes also exhibited differential chromatin opening states in PP and anterior Endo lineages (Figures 5E-5G and S8F-S8I).

Previous study reported that Nodal signaling can boost chromatin accessibility both *in vivo* and *ex vivo*[44,45] . And we observed that PP displayed a higher Nodal levels compared to Endo

290 cells (Figures S2J and S7E). In this ATAC and RNA-seq dataset, we also observed a higher
291 Nodal score in PP cells (Figures 5H and 5I). Thus, it is possible that the differences in Nodal
292 activity may lead to differential chromatin accessibility states and gene expression level in PP
293 and Endo.

294 To further determine how Nodal siganling levels may differentially influence the gene
295 expression dynamics, we first explored the expression profiles of key markers of anterior
296 mesendoderm in the bulk RNA-seq data of Nodal explants injected with different dosages of
297 Nodal mRNA[22]. We observed that the highest Nodal dosages did not result in further elevation
298 of the expression of the endodermal marker *sox17* (Figure 5J), while higher concentrations of
299 Nodal promoted the expression of *gsc* and *ripply1* (Figure 5J). Importantly, these patterns of
300 differential marker expression in response to Nodal/Activin concentration were not only
301 observed in our Nodal explant model but also validated in a human embryonic stem cell system
302 (Figure 5K). These findings suggest that Nodal signaling levels play a conserved role in
303 determining the cell fate specification, which influences the differentiation towards either Endo
304 or PP lineages. To further validate this finding, we injected different dosages of Nodal mRNA
305 into one zebrafish animal pole blastomere at the 128-cell stage, and performed HCR co-staining
306 for *sox32* and *frzb* at 6 hpf (Figure S9A). By quantifying the cell numbers of Endo and the area
307 sizes of PP cluster, we found that moderate concentration of Nodal levels promoted Endo cell
308 specification (Figures S9B-S9E).

309 Based on our aforementioned findings, it becomes evident that subtle variation in Nodal
310 signaling levels may regulate PP and Endo gene expression. This variation is likely regulated
311 by Nodal-Lefty regulatory loops, and contributes to the establishment of distinct chromatin
312 states and transcriptional response of key transcriptional regulators within these two lineages.
313

314 **Gsc and Ripply1 collaborate to suppress the specification of anterior Endo in zebrafish.**
315 It has been reported that endoderm differentiation could be suppressed by upregulation of *gsc*[18],
316 while the role of *ripply1* in endoderm development remains unknown, though it has been
317 characterized as a transcriptional repressor [46,47]. Moreover, both Gsc and Ripply1 are capable
318 of inducing a secondary axis formation when overexpressed in the ventral side of zebrafish

embryos[19,22]. Combining these findings from literature with our observation of high expression of *ripply1* in PP of Nodal explants and zebrafish embryos at 6 hpf (Figures 5D and S8I), we hypothesized that Ripply1 may also play a role in suppressing Endo specification. To test this hypothesis, we generated mutant lines for *gsc* and *ripply1* in zebrafish (Figure 6B). In order to comprehensively analyze the regulatory role of Ripply1 in cooperation with Gsc in the specification of cell fates between PP and Endo cells, we conducted a self-cross of the Tg($gsc^{+/-}$;$ripply1^{+/-}$) lines (Figure 6A). Subsequently, we collected the descendant embryos to perform HCR co-staining for *frzb* and *sox32,* along with genotyping (Figure 6A). From the descendant embryos, we obtained a total of 9 genotypes with different phenotypes displaying variable defects in PP and anterior Endo separation (Figures 6C and S10A). Interestingly, we observed an increase in the number of anterior Endo cells with the loss of wild-type alleles of *gsc* and *ripply1* (Figures 6D, S10B, and S10C). To further investigate the mechanisms of Ripply1 suppressing anterior Endo specification in zebrafish, we injected *ripply1* mRNA at 1-cell stage in zebrafish embryos and found that Endo cell number was dramatically decreased as shown by whole-mount *in situ* hybridization (WISH) of *sox32* (Figure 6F). Additionally, we constructed a plasmid that contained *ripply1* cDNA downstream of the *sox17* promoter. Injection of this plasmid at 1-cell stage also resulted in a decrease in Endo specification shown by EGFP expression (Figure 6E). Taken together, these results demonstrated that Ripply1 acted as an Endo repressor in zebrafish.

It is well established that Gsc functions as an Endo suppressor by directly binding to the promoter region of *sox17*[18]. However, the mechanism by which Ripply1 suppresses Endo specification remains unknown. To address this question, we injected HA-tagged *ripply1* mRNA into zebrafish embryos for conducting CUT&Tag experiments (Figures 6G, S11A and S11B). The CUT&Tag sequencing dataset was analysed following the standard process (Figures S11C-S11H), and 72,683 peaks were enriched in HA-*ripply1* injected samples (Figure 6H). Genes nearby the differentially enriched peaks were used to perform GO enrichment analysis (Figure 6I). Notably, we observed significant enrichment of terms related to “muscle structure development”, “skeletal system development” and “connective tissue development” (Figure 6I), which were consistent with the well-established functions of Ripply1 reported in

348 the published studies[46-48]. Additionally, we also observed significant enrichment of GO terms
349 such as "regulation of cell differentiation", "negative regulation of signaling" and "negative
350 regulation of transcription by RNA polymerase II" (Figure 6I), further supporting the
351 transcriptional repressive function of Ripply1. More interestingly, Ripply1 binding peaks were
352 found to be enriched in the immediate upstream region of the gene body of *sox17* and *sox32*
353 (Figures 6J and 6K), suggesting a direct function of Ripply1 in the transcriptional regulation of
354 these two endodermal markers.

355 In summary, our data proposes a model within PP and anterior Endo lineage separation.
356 Variations of Nodal activities promote the establishment of distinct chromatin states in PP and
357 anterior Endo lineages, which is facilitated by SWI/SNF complexes. These differential
358 chromatin accessibility patterns, in turn, drive the differential expression of key regulators such
359 as *gsc* and *ripply1* in PP and Endo lineages. Collectively, these regulators collaborate to finely
360 regulate the segregation of mesendoderm cell fates (Figure 7).

361

362 **Discussion:**

363 In this study, we delved into the intricacies of specifying and segregating PP and anterior Endo
364 lineages in zebrafish through single-cell multi-omics and live imaging analyses. Our findings
365 revealed the origin of anterior Endo from PP progenitors and unveiled a correlation between
366 subtle differences of Nodal signaling levels and lineage commitment. These signaling
367 variations were identified as potential regulators influencing the expression of cell-fate-specific
368 genes at both epigenetic and transcriptional levels, with the collaboration of SWI/SNF
369 complexes. Through gain-/loss-of-function studies, we demonstrated the collaborative
370 suppression of Gsc and Ripply1 in anterior Endo specification.

371 While the induction of mesendodermal cell fates has been extensively studied[9,12,49,50], the
372 mechanisms underlying the separation of meso- and endo-lineages from common progenitors
373 remain a subject of ongoing research. The widely accepted notion posits that high Nodal
374 signaling levels promote endoderm specification, while lower levels induce mesoderm[11-13].
375 These quantitative effects of Nodal signaling lead to differential activation of transcriptional
376 targets which have differential sensitivity to Nodal activation[2,38]. However, recent studies

challenge this perspective, proposing that Nodal signal level may not strictly determine cell fate separation of mesendoderm. Instead, Nodal signaling provides competency for mesendodermal progenitors to stochastically switch and commit to lineage-specific fates in zebrafish[16]. Moreover, the duration of Nodal signaling has been implicated in specifying different cell fates of mesendoderm, with prolonged signaling promoting prechordal plate specification and suppressing endoderm induction[18]. Besides, other important signaling pathways in early embryonic development also interact with Nodal signaling to regulate cell fate separation[13,32]. It has been well established that Fgf signaling plays a crucial role in regulating cell fate switching between endoderm and mesoderm in lateral margin of zebrafish embryo. In our current work, we preliminarily explored whether Fgf siganling plays roles in regulating cell fate segregation between PP and anterior Endo cells (Figure S12). We observed that several genes related to Fgf siganling were highly enriched in PP and Endo cells (Figure S12B), and inhibition of Fgf signaling could obviously increase the cell number of anterior Endo (Figures S12A and S12C). The findings above suggest that Fgf signaling inhibits the specification of anterior Endo from PP progenitors in zebrafish, which is a similar process to the suppression observed during lateral endoderm specification. However, further investigation is required to understand the specific interactions between Fgf signaling[51] and factors such as Gsc, Ripply1, Sox32[52,53] and the SWI/SNF complexes, as well as their roles in regulating the fate diversification of PP and Endo lineages.

Our study contributed a new layer of understanding to the regulation of mesendodermal cell fate segregation by Nodal signaling. We proposed that Nodal signaling may influence chromatin remodeling factors, thereby affecting the chromatin accessibility states of key regulators such as *gsc* and *ripply1*. It is worth noting that *gsc* and *ripply1* have been identified as direct targets of Nodal signaling[22]. This suggests that the transcription of these genes may directly and sensitively respond to variations in Nodal signaling levels. Based on this understanding, we hypothesize that Nodal signaling can achieve more precise and robust control over the fate segregation of closely related cell types by introducing an additional layer of epigenetic regulatory mechanisms. Additionally, our findings underscored the pivotal role of chromatin openness in morphogen interpretation during development, emphasizing the need to

consider chromatin structure when studying how morphogen gradients regulate patterning formation across different species.

In our work, combining single-cell multi-omics analyses with perturbation experiments, we revealed that chromatin remodeling together with Nodal morphogen promoted the PP and Endo separation in zebrafish. However, which and how chromatin remodeling factors respond to Nodal siganling to facilitate fate diversification remains largely unknown. Our current study identified a key member of SWI/SNF complexes, *srcap*, which is differentially expressed in PP and Endo cells. What triggers the transcriptional difference of *srcap* in these two lineages is still a open question. One of the hypotheses is that the transcription of *srcap* is very sensitive to Nodal signaling (Nodal concentration or Nodal duration), and a little variance in Nodal signaling can drive differential activation of *srcap*. Another speculation is that the activation of *srcap* needs the assistance of pioneer factors, like forkhead family[41,44], whose binding motifs are particularly accessible in PP cells compared to Endo cells (Figures S8K and S8L). All these hypotheses need to be further determined in future works.

Despite these insights, several questions remain unanswered. Firstly, we discovered a potential role of Nodal activity levels in the separation of PP and Endo cells. However, further investigation is required to understand how Nodal activity levels and signaling duration are integrated to regulate this process. Secondly, although our study determined the cooperative role of Gsc and Ripply1 in suppressing endoderm specification, the potential involvement of other unidentified transcriptional repressors, as suggested in previous work[18], warrants further investigation. Notably, even in double homozygous mutants of *gsc* and *ripply1*, the specification of PP clusters was still detected, and the enrichment of another transcriptional repressor, *osr1*, in PP cells (Figure S8J) suggested a complex network of cooperative endoderm repressors in preventing cells from differentiating into Endo. Thus, it would be worth studying how Gsc, Ripply1, Osr1 and other potential factors cooperatively regulate PP and Endo specification in the future. Lastly, the anterior endoderm and ventral-lateral endoderm were mixed together in our single-cell ATAC-seq dataset, which brought in interferences when we interpreted the mechanisms of the separation between PP and anterior Endo. More replicates of embryonic single-cell multi-omics or performing single-cell multi-omics on Nodal explants

may help to address this issue in future studies.

Methods:

Animal ethics

Zebrafish strains were conducted following standard procedures, and experimental procedures were approved by the Institutional Review Board of Zhejiang University. The protocol number is ZJU20220375.

Generation of Nodal explants

Nodal explant was generated as our previous work described[54]. 10 pg *ndr2* mRNA was injected into one blastomere of zebrafish embryonic animal pole at the 128-cell stage. About half of the animal pole region of the embryo was cut off from the blastula at the 1k-cell stage, and was cultured in a Petri dish coated with 1.5% agarose gel filled with Dulbecco's modified Eagle's medium/nutrient mixture F-12 (DMEM/F-12) with 10 mM HEPES, 1x minimum essential medium (MEM) containing non-essential amino acids and supplemented with 7 mM $CaCl_2$, 1 mM sodium pyruvate, 50 μg/ml gentamycin, 100 μM 2-mercaptoethanol, 1× antibiotic-antimycotic (15240062, Thermo Fisher) and 10% serum replacement. For generating *ndr1*-morphant Nodal explants, *ndr1* morpholino (0.5 mM, 2 nL) was injected into yolk of wild-type zebrafish embryos at 1-cell stage; while for generating *lft1*-mutant Nodal explants, the embryos of *lft1* mutants were used to construct Nodal explants. The sequence of *ndr1* morpholino was 5' - ATGTCAAATCAAGGTAATAATCCAC - 3'.

Live imaging

Tg(*gsc*:EGFP;*sox17*:dsRed) embryos and Nodal explants generated from those embryos were used to perform live imaging analysis. 0.5% low-melt agarose was used to mount the embryos or Nodal explants in glass-bottom dishes (Cellvis, D35-20-0-N). The embryos or explants were live-imaged by confocal laser scanning microscopy (OLYMPUS FV12-IXCOV) using a 20X objective lens or a 40X oil immersion lens.

***In situ* hybridization chain reaction (HCR)**

465 HCR co-staining of *frzb*, *sox32* and *gsc* was performed as previous studies described[21]. The
466 probes of those genes were ordered and produced from Molecular Technologies
467 (http://www.moleculartechnologies.org/). Embryos were fixed in DEPC-treated PBS with
468 4%(w/v) paraformaldehyde at 4°C overnight. The embryos were incubated in 500 μL 30%
469 formamide probe hybridization with 2 pmol of each HCR probe set at 37°C overnight. Next
470 day, 30% formamide probe wash buffer was used to stop hybridization by repeated washing of
471 the embryos at 37°C. Fluorescent signals were generated and amplified by probes that bound
472 to fluorescent HCR amplifiers in an amplification buffer overnight at room temperature. To halt
473 this process, the samples were washed several times using 5× SSC with 0.001% Tween 20. The
474 reaction buffers, fluorescent hairpins and probes were manufactured by Molecular
475 Technologies. OLYMPUS FV12-IXCOV confocal microscope was used to photograph those
476 HCR co-staining samples.
477
478 **Double-color RNA-fluorescence *in situ* hybridization (FISH)**
479 Double-color FISH of *gsc* and *sox17* was conducted according to the protocol from manufactory
480 (http://www.pinpoease.com/, GD Pinpoease Biotech Co., Ltd.). Wild-type embryos or Nodal
481 explants (6 hpf, 7 hpf and 8 hpf) were fixed in DEPC-treated PBS with 4%(w/v) paraformaldehyde
482 at 4°C overnight. Pre-A solution was used to inhibit the peroxidase activity. Target RNA molecules
483 were exposed through protease treatment, followed by hybridization with probes at 4°C for 2 hours.
484 The fluorescent signal was amplified through sequential reactions 1, 2, and 3. Lastly, a tyramide
485 fluorescent substrate (OpalTM520, Akoya Biosciences) was used to incubate the embryos, enabling
486 fluorescent labeling of the target RNA through the Tyramide Signal Amplification (TSA) assay.
487
488 **Immunostaining and quantification of pSmad2**
489 Samples were fixed at 4% paraformaldehyde overnight for pSmad2/3 immunostaining. The
490 experiment was performed as previously described[54]. Confocal laser scanning microscopy
491 (OLYMPUS FV12-IXCOV) was used to scan the immunostained samples. Imaris (Version 9.7)
492 software was used to quantify the signaling activity of pSmad2 (488 nm), RFP (561 nm) and DAPI
493 (405 nm). Firstly, the raw image data was loaded in Imaris and visualized in a three-dimensional
494 (3D) view. The Spot plugin from Imaris was used to detect spots with pSmad2 signal. The diameter

495 of spot detection was set to 5-6 μm for GFP channel. The spots were automatically identified with
496 default parameters. And then, as the identification of some spots was inaccurate, we manually added
497 or removed some spots. Lastly, the coordinates and signal intensities of each spot were exported for
498 next-step analyses. To make all images comparable, we used DAPI signal as an internal control to
499 normalize the signal intensity in other channels. When plotting a pSmad2 signal intensity gradient
500 along a distance, the cell with the highest pSmad2 signal was assigned as the start point, and then
501 the distance of other cells was calculated by comparing them with the start point cell. The fitting
502 curve was plotted by ggplot2[55] in R (https://www.r-project.org).
503
504 **Whole-mount *in situ* hybridization (WISH)**
505 The processes of WISH and the construction of *sox32* probes were described in our previous work[54].
506 Embryos were fixed in DEPC-treated PBS with 4%(w/v) paraformaldehyde at 4°C overnight. To
507 enable long-term storage, the embryos were dehydrated using 100% methanol. For WISH
508 experiments, probes were labeled with digoxigenin-11-UTP (Roche Diagnostics), and the substrate
509 was NBT/BCIP.
510
511 **Activation of Activin/Nodal signaling in human embryonic stem cell system**
512 Human embryonic stem cell (hESC) lines were used between passage 45-50. Cells were seeded
513 equally on matrigel-coated plate and cultured in mTeSR medium. Before the experiment, each group
514 was pretreated in N2B27 medium for 6 hours. Then the control group was maintained in N2B27,
515 while the experiment groups were cultured in N2B27 medium supplemented with different
516 concentrations of Activn-A (0, 10, 40, 70 and 100 ng/mL). The cellular RNA of each group was
517 extracted with Trizol after 12 hours of treatment.
518
519 **Overexpression of *gsc* and *ripply1* in zebrafish embryos**
520 The mRNA of *gsc* and *ripply1* (synthesized *in vitro*) and *sox17* promotor-driven *ripply1* plasmid
521 were co-injected into zebrafish embryos at 1-cell stage. The ddH_2O was injected as control. The
522 embryos were imaged or fixed at 8 hpf. The *sox32* probe was used for WISH.
523
524 **Generating heterozygous embryos of *gsc* and *ripply1***

525 The *ripply1* mutants were obtained from Dr. Ming Shao's lab at Shandong University. We
526 knockout *gsc* in *ripply1*-mutant embryos by CRISPR-Cas9 system. F0 embryos were raised up,
527 and then crossed with wild-type (AB). The descendant embryos (F1) were raised up and
528 genotyped. The adult zebrafish of the target genotype were selected.
529
530 **Quantifying the cell number of anterior Endo**
531 Imaris (version 9.7) was used to identify the Endo cells based on the HCR images. Briefly, the raw
532 image data was imported into Imaris, and the object was visualized in a 3D view. The Spot plugin
533 from Imaris was used to detect each cell. The diameter of spot detection was set to 10-12 μm for
534 GFP channel (staining for *sox32* or *sox17*). The candidate spots were selected by setting an
535 appropriate quality threshold. Finally, the coordinates and signal intensities of each spot were
536 exported from Imaris and used for further analysis.
537
538 **CUT&Tag sample preparation**
539 HA-*ripply1* sequence with homologous sequences was generated through two PCR steps using
540 two separate sets of primers (Table S1, reverse primer was common, *ripply1*-F1 primer:
541 tcaaggcctctcgagcctctagaATGTACCCATACGATGTTCCAGATTACGCT; *ripply1*-F2 primer:
542 ACGATGTTCCAGATTACGCTGGCAGCATGAATTCTGTGTGCTTTGCCACT; *ripply1*-R
543 primer: TACGACTCACTATAGTTCTAGAtcagttgaaagctgtgaagtga). The details of generating
544 mRNA *in vitro* was described in our previous protocol[21]. Briefly, the HA-*ripply1* PCR products
545 were inserted into pCS^{2+} plasmid through homologous recombination using ClonExpress II One
546 Step Cloning Kit. The plasmid containing HA-*ripply1* was linearized using *Not1* cleavage, and
547 HA-*ripply1* mRNA were generated through mRNA *in vitro* synthesis using mMESSAGE
548 mMACHINETM SP6 transcription kit. Wild-type embryos were injected with HA-*ripply1*
549 mRNA or ddH_2O at one-cell stage and harvested at 6 hpf. Yolk was removed through pipetting,
550 and the cells were collected. The cell viability was assessed by Trypan blue staining and the
551 cell number was then counted.
552
553 **CUT&Tag experiment**

554 CUT&Tag was performed on samples of wildtype, HA-*ripply1*-injected and HA-ripply1-
555 injected without primary antibody using Hyperactive Universal CUT&Tag Assay Kit for
556 Illumina Pro (Vazyme, TD904), and each sample had two replicates. Briefly, around 100,000
557 cells were collected and immobilized on Concanavalin A-coat Magnetic Beads. Cells were then
558 incubated with primary antibody (HA-Tag Rabbit mAb, Cell Signaling Technology, 3724S,
559 1:50 dilution) at 4°C for 12 h-16 h. Tethered cells were washed thoroughly to remove excessive
560 primary antibody and incubated with secondary antibody (Goat Anti-Rabbit IgG H&L, Vazyme,
561 Ab207-01, 1:100 dilution) for 60 minutes at room temperature. Then samples were washed
562 thoroughly to remove unbound secondary antibody and incubated with pA/G-Tnp for 1 hour at
563 room temperature. DNA was then fragmentated through Trueprep Tagment Buffer L (TTBL).
564 Fragmented DNA was extracted using DNA extract beads and amplified through PCR. PCR
565 products were purified using VAHTS DNA CLEAN Beads (Vazyme, N411) and then sent to
566 Novogene Co., Ltd. (Beijing, China) for sequencing. Paired-end sequencing at 150 bp read
567 length was performed on an NovaSeq 6000 System.
568
569 **CUT&Tag analysis**
570 Sequencing data of CUT&Tag samples were first treated by Cutadapt v4.5[56] to remove adapters
571 and trim reads using the following parameters "*-m 18 -q 30,30 --max-n=0.05 -e 0.2 -n 2*". The
572 trimmed reads were then aligned to zebrafish genome (danRer11) through Bowtie2 v2.5.2[57]
573 using the following parameters "*--end-to-end --very-sensitive --no-mixed --no-discordant --*
574 *phred33 -I 10 -X 700*". Samtools v1.18[58] and BEDtools v2.31.0[59] were then used for post-
575 alignment processing to covert file formats in preparation for the peak calling and visualization.
576 BigWig tracks were generated for visualization of chromatin landscapes in interested regions
577 using the Integrative Genomics Viewer (IGV)[60]. To assess the reproducibility between
578 replicates, the genome was spilt into 500 bp bins, and a Pearson correlation of the log_2-
579 transformed read counts in each bin was calculated between datasets.
580 SEACR[61] was used to call "non stringent" peaks for wild-type and HA-*ripply1*-injected samples
581 using merged HA-*ripply1*-injected samples without primary antibody as control. Additionally,
582 top 1% of enrich regions were selected as peaks by AUC without controls. Peaks were annotated

583 by ChIPpeakAnno v3.34.1[62] using UCSC annotation from
584 TxDb.Drerio.UCSC.danRer11.refGene v3.4.6[63]. Significantly enriched peaks in HA-*ripply1*-
585 injected samples were identified using DESeq2 v1.40.2[64], and enriched GO terms were
586 identified using clusterProfiler v4.9.0.2[65]. Signal intensity heatmaps were generated using
587 deeptools v3.5.4[66]. The peaks of HA-*ripply1*-injected rep1 were used as the reference to
588 generate computeMatrix using the *reference-point* model (*--skipZeros --*
589 *afterRegionStartLength 3000 --beforeRegionStartLength 3000 --referencePoint center*), and
590 *PlotHeatmap* function was used to plot signal intensity.
591
592 **Processing and analyzing single-cell RNA-seq data**
593 Illumina sequencing reads were aligned to the reference genome (GRCz11) of zebrafish through
594 10× Genomics CellRanger pipeline (version 3.0.2) with default parameters. Nodal explants
595 generated from *lft1* mutants and *ndr1* morphants yielded 5,419 and 5,195 cells respectively. The
596 expression matrix of each sample was obtained via CellRanger pipeline analysis and used for further
597 analysis. The single-cell RNA-seq data of wild-type Nodal explants was reused from our previous
598 study[54].
599
600 **Processing and analyzing single-cell multi-omics data**
601 Illumina sequencing reads were aligned to the reference genome (GRCz11) of zebrafish using 10×
602 Genomics CellRanger-arc pipeline (version 2.0.0) with default parameters. Expression matrix and
603 fragments files were obtained after running the pipeline. 4,879 cells were obtained. Signac[67] was
604 used for downstream analyses with default parameters. Low-quality cells were filtered out with
605 nCount_ATAC < 100000 & nCount_RNA < 50000 & nCount_ATAC > 1000 & nCount_RNA >
606 1000 & nucleosome_signal < 2 & TSS.enrichment > 1 & percent.mt < 4. And then, gene expression
607 data and DNA accessibility data were processed respectively by Signac with default parameters.
608 The RNA expression level was utilized to identify cluster markers for cell annotation. Gene activity
609 matrix was obtained by assessing the chromatin accessibility associated with each gene through
610 *GeneActivity* function.
611
612 **Differential expression analysis of PP cells between wild-type, *lft1*-mutant and *ndr1*-morphant**
613 **Nodal explants**

614 The three sing-cell RNA-seq datasets of Nodal explants constructed from wild-type embryos, *lft1*
615 mutants and *ndr1* morphants were integrated by Seurat[68]. To investigate the functional and
616 regulatory effects of Nodal signals on cell differentiation, we compared the wild-type mesoderm PP
617 cells to the mesoderm PP cells in *lft1* mutants and *ndr1* morphants respectively, and differentially-
618 expressed (DE) genes were identified through Seurat v4.0.2 (https://github.com/satijalab/seurat)
619 with a Bonferroni adjusted p-value < 0.05. As it is known that EVL is not affected by Nodal
620 signaling[54,69], DE genes identified in EVL were regarded as background noises and were removed
621 from the mesoderm PP DE genes. The mesoderm PP DE genes positively correlated with Nodal
622 concentration were then selected, constructing two gene sets: upregulated DE genes in *lft1* mutants
623 and downregulated DE genes in *ndr1* morphants. GO enrichment analysis was performed on these
624 two gene sets respectively using clusterProfilter v4.2.2 (https://github.com/YuLab-
625 SMU/clusterProfiler). The enriched GO terms in "biological process" subontology were identified
626 using a Benjamini-Hochberg adjusted p-value < 0.05.
627
628 **Cell-cell communication analysis by LIANA**
629 R package, LIANA[31] v0.1.5 (https://github.com/saezlab/liana/), was used for the investigation of
630 ligand-receptor interactions among different cell types. The ligand-receptor analysis was performed
631 against the ligand-receptor reference achieved from Omnipath resource using 5 different methods
632 implemented in LIANA, including Natmi, Connectome, SingleCellSingalR, iTALK and
633 CellPhoneDBv2. The consensus rank aggregated from the results of these methods was used for the
634 identification of enriched ligand-receptor interactions.
635
636 **Inferring cell-cell communication by CellChat**
637 CellChat[70] was employed to systematically analyze cell-cell communication based on prior
638 known zebrafish ligand-receptor interaction database CellChatDB. As some known interactions
639 were missing in the database, we manually added some interactions of interest into the database.
640 The expression data of scRNA-seq was preprocessed to identify over-expressed ligands and
641 receptors for each group. CellChat inferred communication probability between two interacting
642 cell groups based on the average gene expression of a ligand in one cell group and the average
643 gene expression of a receptor in another cell group. The communication probabilities of

signaling pathways were then calculated by summarizing the communication probabilities of all ligands-receptors interactions associated with each pathway.

Gene set enrichment analysis

The wild-type mesoderm PP gene expression was compared to the mesoderm PP gene expression of *lft1* mutants and *ndr1* morphants respectively using Seurat v4.0.2 (https://github.com/satijalab/seurat). The genes expressed in more than 10% cells in either of the two compared populations were retained. A ranked list was formed on the retained genes using sign($\log_2$FC) * (-$\log_{10}$PValue) as the ranking statistic. The mapping between GO terms and zebrafish genes was achieved through org.Dr.eg.db v3.14.0 (https://bioconductor.org/packages/org.Dr.eg.db/). GSEA was performed on the selected GO terms by clusterProfiler v4.2.2 (https://github.com/YuLab-SMU/clusterProfiler), using fgsea (https://github.com/ctlab/fgsea) with 10^5 interactions. R package, enrichplot v1.14.2 (https://github.com/YuLab-SMU/enrichplot), was then used to visualize the GSEA results.

Single-cell RNA-seq trajectory analysis

Three different methods were used to perform single-cell RNA-seq trajectory analysis. The developmental trajectory tree of zebrafish embryos and Nodal explants was constructed by URD[71] with default parameters as described in previous studies[71]. The branchpoint preference plot of PP and Endo was constructed by URD with default parameters. Firstly, *branchpointPreferenceLayout* function was used to define the preference layout for the branchpoint. And then stage, pseudotime information and gene expression were plotted on the branchpoint using *plotBranchpoint* function. The expression matrix of PP and Endo cells was also used to construct trajectory tree by monocle2[28] and monocle3[72] with default parameters. And differential expression analysis was performed at the branching point of PP and Endo separation on trajectory tree constructed by *BEAM* function in monocle2. Modules of co-regulated genes along PP or Endo differentiation lineage were identified by *find_gene_modules* function in monocle3 with default parameters. The cells contributed to the preference layout for the Endo and PP brachpoint from URD analysis were also selected as inputs for Palantir[27]. We used Harmony[73] to calculate the augmented affinity matrix for data of all time points. Data was visualized using force directed layouts. Palantir was used for downstream analysis,

674 and a *nanog*^{high} cell was used as the start cell. A *frzb*^{high} cell (PP) and a *sox17*^{high} cell (Endo) were
675 selected as the terminal cells. Endo and PP cell differential trajectory was detected by
676 *palantir.core.run_palantir* function from Palantir. And finally, gene expression trend along Palantir
677 inferred pseudotime was calculated by *palantir.presults.compute_gene_trends* function.
678
679 **Calculating Nodal score in single-cell RNA-seq data**
680 Nodal functions through activating a set of key downstream genes in a concentration-dependent
681 manner. Our previous study identified 105 Nodal immediate target genes by analyzing bulk RNA-
682 seq datasets of Nodal mRNA injected explants[22]. We overlapped these 105 genes with 61 Nodal
683 direct targets, which were previously identified through ChIP-seq analysis of pSmad2[38]. This
684 analysis allowed us to pinpoint 29 Nodal downstream genes whose expression was highly sensitive
685 to Nodal activity. To quantify Nodal activity, we defined a Nodal score based on its downstream
686 transcriptional response. This score was calculated by regressing out the expression levels of these
687 29 Nodal downstream genes. To accomplish this, the *AddModuleScore* function in Seurat was
688 employed.
689
690 **Data availability**
691 The data generated in this study is deposited in the Gene Expression Omnibus (GEO). The single-
692 cell RNA sequencing and single-cell multi-omics data is under accession number GSE223636, and
693 the CUT&Tag data is under the accession number GSE249292.
694
695 **Code availability**
696 Any custom code and data are available from the authors upon request. All analyses are based on
697 previously published code and software.
698
699 **Additional information**
700 Supplemental Information: Supplementary Figures 1-12, Supplementary Table S1, Supplementary
701 Data 1-8 and Supplementary Movies 1-3.
702
703

Refference:

1. Schier, A.F., and Talbot, W.S. (2005). Molecular genetics of axis formation in zebrafish. Annual review of genetics *39*, 561-613. 10.1146/annurev.genet.37.110801.143752.
2. Jones, W.D., and Mullins, M.C. (2022). Cell signaling pathways controlling an axis organizing center in the zebrafish. Current topics in developmental biology *150*, 149-209. 10.1016/bs.ctdb.2022.03.005.
3. Gurdon, J.B., and Bourillot, P.Y. (2001). Morphogen gradient interpretation. Nature *413*, 797-803. 10.1038/35101500.
4. Xu, P.F., Houssin, N., Ferri-Lagneau, K.F., Thisse, B., and Thisse, C. (2014). Construction of a vertebrate embryo from two opposing morphogen gradients. Science (New York, N.Y.) *344*, 87-89. 10.1126/science.1248252.
5. Xu, P.F., Borges, R.M., Fillatre, J., de Oliveira-Melo, M., Cheng, T., Thisse, B., and Thisse, C. (2021). Construction of a mammalian embryo model from stem cells organized by a morphogen signalling centre. Nature communications *12*, 3277. 10.1038/s41467-021-23653-4.
6. Chen, Y., and Schier, A.F. (2001). The zebrafish Nodal signal Squint functions as a morphogen. Nature *411*, 607-610. 10.1038/35079121.
7. Schier, A.F. (2009). Nodal morphogens. Cold Spring Harbor perspectives in biology *1*, a003459. 10.1101/cshperspect.a003459.
8. Hill, C.S. (2018). Spatial and temporal control of NODAL signaling. Current opinion in cell biology *51*, 50-57. 10.1016/j.ceb.2017.10.005.
9. Schier, A.F. (2003). Nodal signaling in vertebrate development. Annual review of cell and developmental biology *19*, 589-621. 10.1146/annurev.cellbio.19.041603.094522.
10. Feldman, B., Gates, M.A., Egan, E.S., Dougan, S.T., Rennebeck, G., Sirotkin, H.I., Schier, A.F., and Talbot, W.S. (1998). Zebrafish organizer development and germ-layer formation require nodal-related signals. Nature *395*, 181-185. 10.1038/26013.
11. Thisse, B., Wright, C.V., and Thisse, C. (2000). Activin- and Nodal-related factors control antero-posterior patterning of the zebrafish embryo. Nature *403*, 425-428. 10.1038/35000200.
12. Dougan, S.T., Warga, R.M., Kane, D.A., Schier, A.F., and Talbot, W.S. (2003). The role of the zebrafish nodal-related genes squint and cyclops in patterning of mesendoderm. Development (Cambridge, England) *130*, 1837-1851. 10.1242/dev.00400.
13. van Boxtel, A.L., Economou, A.D., Heliot, C., and Hill, C.S. (2018). Long-Range Signaling Activation and Local Inhibition Separate the Mesoderm and Endoderm Lineages. Developmental cell *44*, 179-191.e175. 10.1016/j.devcel.2017.11.021.
14. Martyn, I., Kanno, T.Y., Ruzo, A., Siggia, E.D., and Brivanlou, A.H. (2018). Self-organization of a human organizer by combined Wnt and Nodal signalling. Nature *558*, 132-135. 10.1038/s41586-018-0150-y.
15. Poulain, M., Fürthauer, M., Thisse, B., Thisse, C., and Lepage, T. (2006). Zebrafish endoderm formation is regulated by combinatorial Nodal, FGF and BMP signalling. Development (Cambridge, England) *133*, 2189-2200. 10.1242/dev.02387.
16. Economou, A.D., Guglielmi, L., East, P., and Hill, C.S. (2022). Nodal signaling establishes a competency window for stochastic cell fate switching. Developmental cell *57*, 2604-2622 e2605. 10.1016/j.devcel.2022.11.008.

17. Barone, V., Lang, M., Krens, S.F.G., Pradhan, S.J., Shamipour, S., Sako, K., Sikora, M., Guet, C.C., and Heisenberg, C.P. (2017). An Effective Feedback Loop between Cell-Cell Contact Duration and Morphogen Signaling Determines Cell Fate. Developmental cell *43*, 198-211.e112. 10.1016/j.devcel.2017.09.014.
18. Sako, K., Pradhan, S.J., Barone, V., Inglés-Prieto, Á., Müller, P., Ruprecht, V., Čapek, D., Galande, S., Janovjak, H., and Heisenberg, C.P. (2016). Optogenetic Control of Nodal Signaling Reveals a Temporal Pattern of Nodal Signaling Regulating Cell Fate Specification during Gastrulation. Cell reports *16*, 866-877. 10.1016/j.celrep.2016.06.036.
19. Dixon Fox, M., and Bruce, A.E. (2009). Short- and long-range functions of Goosecoid in zebrafish axis formation are independent of Chordin, Noggin 1 and Follistatin-like 1b. Development (Cambridge, England) *136*, 1675-1685. 10.1242/dev.031161.
20. Seiliez, I., Thisse, B., and Thisse, C. (2006). FoxA3 and goosecoid promote anterior neural fate through inhibition of Wnt8a activity before the onset of gastrulation. Developmental biology *290*, 152-163. 10.1016/j.ydbio.2005.11.021.
21. Cheng, T., Xing, Y.Y., Dong, Y., and Xu, P.F. (2023). Protocol for generation and assessment of head-like structure in zebrafish. STAR Protoc *4*, 102553. 10.1016/j.xpro.2023.102553.
22. Cheng, T., Xing, Y.Y., Liu, C., Li, Y.F., Huang, Y., Liu, X., Zhang, Y.J., Zhao, G.Q., Dong, Y., Fu, X.X., et al. (2023). Nodal coordinates the anterior-posterior patterning of germ layers and induces head formation in zebrafish explants. Cell reports *42*, 112351. 10.1016/j.celrep.2023.112351.
23. Warga, R.M., and Nüsslein-Volhard, C. (1999). Origin and development of the zebrafish endoderm. Development (Cambridge, England) *126*, 827-838.
24. Wagner, D.E., Weinreb, C., and Collins, Z.M. (2018). Single-cell mapping of gene expression landscapes and lineage in the zebrafish embryo. Science (New York, N.Y.) *360*, 981-987. 10.1126/science.aar4362.
25. Farrell, J.A., and Wang, Y. (2018). Single-cell reconstruction of developmental trajectories during zebrafish embryogenesis. Science (New York, N.Y.) *360*. 10.1126/science.aar3131.
26. Becht, E., and McInnes, L. (2018). Dimensionality reduction for visualizing single-cell data using UMAP. Nature biotechnology. 10.1038/nbt.4314.
27. Setty, M., Kiseliovas, V., Levine, J., Gayoso, A., Mazutis, L., and Pe'er, D. (2019). Characterization of cell fate probabilities in single-cell data with Palantir. Nature biotechnology *37*, 451-460. 10.1038/s41587-019-0068-4.
28. Qiu, X., Mao, Q., Tang, Y., Wang, L., Chawla, R., Pliner, H.A., and Trapnell, C. (2017). Reversed graph embedding resolves complex single-cell trajectories. Nature methods *14*, 979-982. 10.1038/nmeth.4402.
29. Zhou, Y., Zhou, B., Pache, L., Chang, M., Khodabakhshi, A.H., Tanaseichuk, O., Benner, C., and Chanda, S.K. (2019). Metascape provides a biologist-oriented resource for the analysis of systems-level datasets. Nature communications *10*, 1523. 10.1038/s41467-019-09234-6.
30. Xia, P., Gutl, D., Zheden, V., and Heisenberg, C.P. (2019). Lateral Inhibition in Cell Specification Mediated by Mechanical Signals Modulating TAZ Activity. Cell *176*, 1379-1392 e1314. 10.1016/j.cell.2019.01.019.
31. Dimitrov, D., Turei, D., Garrido-Rodriguez, M., Burmedi, P.L., Nagai, J.S., Boys, C., Ramirez Flores, R.O., Kim, H., Szalai, B., Costa, I.G., et al. (2022). Comparison of methods and

792 resources for cell-cell communication inference from single-cell RNA-Seq data. Nature
793 communications *13*, 3224. 10.1038/s41467-022-30755-0.
794 32. Mathieu, J., Griffin, K., Herbomel, P., Dickmeis, T., Strahle, U., Kimelman, D., Rosa, F.M., and
795 Peyrieras, N. (2004). Nodal and Fgf pathways interact through a positive regulatory loop
796 and synergize to maintain mesodermal cell populations. Development (Cambridge,
797 England) *131*, 629-641. 10.1242/dev.00964.
798 33. Müller, P., Rogers, K.W., Jordan, B.M., Lee, J.S., Robson, D., Ramanathan, S., and Schier, A.F.
799 (2012). Differential diffusivity of Nodal and Lefty underlies a reaction-diffusion patterning
800 system. Science (New York, N.Y.) *336*, 721-724. 10.1126/science.1221920.
801 34. Chen, Y., and Schier, A.F. (2002). Lefty proteins are long-range inhibitors of squint-
802 mediated nodal signaling. Current biology : CB *12*, 2124-2128. 10.1016/s0960-
803 9822(02)01362-3.
804 35. Sekine, R., Shibata, T., and Ebisuya, M. (2018). Synthetic mammalian pattern formation
805 driven by differential diffusivity of Nodal and Lefty. Nature communications *9*, 5456.
806 10.1038/s41467-018-07847-x.
807 36. Kuhn, T., Landge, A.N., Morsdorf, D., Cossmann, J., Gerstenecker, J., Capek, D., Muller, P.,
808 and Gebhardt, J.C.M. (2022). Single-molecule tracking of Nodal and Lefty in live zebrafish
809 embryos supports hindered diffusion model. Nature communications *13*, 6101.
810 10.1038/s41467-022-33704-z.
811 37. Liu, L., Nemashkalo, A., Rezende, L., Jung, J.Y., Chhabra, S., Guerra, M.C., Heemskerk, I.,
812 and Warmflash, A. (2022). Nodal is a short-range morphogen with activity that spreads
813 through a relay mechanism in human gastruloids. Nature communications *13*, 497.
814 10.1038/s41467-022-28149-3.
815 38. Dubrulle, J., Jordan, B.M., Akhmetova, L., Farrell, J.A., Kim, S.H., Solnica-Krezel, L., and
816 Schier, A.F. (2015). Response to Nodal morphogen gradient is determined by the kinetics
817 of target gene induction. eLife *4*. 10.7554/eLife.05042.
818 39. Xing, C., Shen, W., Gong, B., Li, Y., Yan, L., and Meng, A. (2022). Maternal Factors and
819 Nodal Autoregulation Orchestrate Nodal Gene Expression for Embryonic Mesendoderm
820 Induction in the Zebrafish. Front Cell Dev Biol *10*, 887987. 10.3389/fcell.2022.887987.
821 40. Pinheiro, D., Kardos, R., Hannezo, E., and Heisenberg, C.P. (2022). Morphogen gradient
822 orchestrates pattern-preserving tissue morphogenesis via motility-driven unjamming.
823 Nature Physics. 10.1038/s41567-022-01787-6.
824 41. Coda, D.M., Gaarenstroom, T., East, P., Patel, H., Miller, D.S., Lobley, A., Matthews, N.,
825 Stewart, A., and Hill, C.S. (2017). Distinct modes of SMAD2 chromatin binding and
826 remodeling shape the transcriptional response to NODAL/Activin signaling. eLife *6*.
827 10.7554/eLife.22474.
828 42. Ross, S., Cheung, E., Petrakis, T.G., Howell, M., Kraus, W.L., and Hill, C.S. (2006). Smads
829 orchestrate specific histone modifications and chromatin remodeling to activate
830 transcription. EMBO J *25*, 4490-4502. 10.1038/sj.emboj.7601332.
831 43. Xiao, L., Parolia, A., Qiao, Y., Bawa, P., Eyunni, S., Mannan, R., Carson, S.E., Chang, Y., Wang,
832 X., Zhang, Y., et al. (2022). Targeting SWI/SNF ATPases in enhancer-addicted prostate
833 cancer. Nature *601*, 434-439. 10.1038/s41586-021-04246-z.
834 44. Coda, D.M., Patel, H., Gori, I., Gaarenstroom, T.E., Song, O.R., Howell, M., and Hill, C.S.
835 (2022). A network of transcription factors governs the dynamics of NODAL/Activin

836 transcriptional responses. Journal of cell science *135*. 10.1242/jcs.259972.
837 45. Akhmetova, L. (2016). Transcriptional Regulation of Nodal Target Genes in Early Zebrafish
838 Development. Doctor (Harvard University).
839 46. Kawamura, A., Koshida, S., Hijikata, H., Ohbayashi, A., Kondoh, H., and Takada, S. (2005).
840 Groucho-associated transcriptional repressor ripply1 is required for proper transition
841 from the presomitic mesoderm to somites. Developmental cell *9*, 735-744.
842 10.1016/j.devcel.2005.09.021.
843 47. Yabe, T., Uriu, K., and Takada, S. (2023). Ripply suppresses Tbx6 to induce dynamic-to-
844 static conversion in somite segmentation. Nature communications *14*, 2115.
845 10.1038/s41467-023-37745-w.
846 48. Windner, S.E., Doris, R.A., Ferguson, C.M., Nelson, A.C., Valentin, G., Tan, H., Oates, A.C.,
847 Wardle, F.C., and Devoto, S.H. (2015). Tbx6, Mesp-b and Ripply1 regulate the onset of
848 skeletal myogenesis in zebrafish. Development (Cambridge, England) *142*, 1159-1168.
849 10.1242/dev.113431.
850 49. Shen, M.M. (2007). Nodal signaling: developmental roles and regulation. Development
851 (Cambridge, England) *134*, 1023-1034. 10.1242/dev.000166.
852 50. Takenaga, M., Fukumoto, M., and Hori, Y. (2007). Regulated Nodal signaling promotes
853 differentiation of the definitive endoderm and mesoderm from ES cells. Journal of cell
854 science *120*, 2078-2090. 10.1242/jcs.004127.
855 51. Mizoguchi, T., Izawa, T., Kuroiwa, A., and Kikuchi, Y. (2006). Fgf signaling negatively
856 regulates Nodal-dependent endoderm induction in zebrafish. Developmental biology
857 *300*, 612-622. 10.1016/j.ydbio.2006.08.073.
858 52. Kikuchi, Y., Agathon, A., Alexander, J., Thisse, C., Waldron, S., Yelon, D., Thisse, B., and
859 Stainier, D.Y. (2001). casanova encodes a novel Sox-related protein necessary and
860 sufficient for early endoderm formation in zebrafish. Genes & development *15*, 1493-
861 1505. 10.1101/gad.892301.
862 53. Aoki, T.O., David, N.B., Minchiotti, G., Saint-Etienne, L., Dickmeis, T., Persico, G.M., Strahle,
863 U., Mourrain, P., and Rosa, F.M. (2002). Molecular integration of casanova in the Nodal
864 signalling pathway controlling endoderm formation. Development (Cambridge, England)
865 *129*, 275-286. 10.1242/dev.129.2.275.
866 54. Cheng, T., Xing, Y.-Y., Li, Y.-F., Liu, C., Huang, Y., Zhang, Y.-J., Megason, S.G., and Xu, P.-
867 F. (2021). Single cell response landscape of graded Nodal signaling in zebrafish explants.
868 bioRxiv. 10.1101/2021.04.25.441305.
869 55. Wickham, H. (2016). ggplot2 : Elegant Graphics for Data Analysis. Use R!,. 2nd ed. Springer
870 International Publishing : Imprint: Springer,.
871 56. Kechin, A., Boyarskikh, U., Kel, A., and Filipenko, M. (2017). cutPrimers: A New Tool for
872 Accurate Cutting of Primers from Reads of Targeted Next Generation Sequencing. J
873 Comput Biol *24*, 1138-1143. 10.1089/cmb.2017.0096.
874 57. Langmead, B., and Salzberg, S.L. (2012). Fast gapped-read alignment with Bowtie 2.
875 Nature methods *9*, 357-359. 10.1038/nmeth.1923.
876 58. Li, H., Handsaker, B., Wysoker, A., Fennell, T., Ruan, J., Homer, N., Marth, G., Abecasis, G.,
877 Durbin, R., and Genome Project Data Processing, S. (2009). The Sequence Alignment/Map
878 format and SAMtools. Bioinformatics (Oxford, England) *25*, 2078-2079.
879 10.1093/bioinformatics/btp352.

880 59. Quinlan, A.R., and Hall, I.M. (2010). BEDTools: a flexible suite of utilities for comparing
881 genomic features. Bioinformatics (Oxford, England) *26*, 841-842.
882 10.1093/bioinformatics/btq033.
883 60. Robinson, J.T., Thorvaldsdottir, H., Turner, D., and Mesirov, J.P. (2023). igv.js: an
884 embeddable JavaScript implementation of the Integrative Genomics Viewer (IGV).
885 Bioinformatics (Oxford, England) *39*. 10.1093/bioinformatics/btac830.
886 61. Meers, M.P., Tenenbaum, D., and Henikoff, S. (2019). Peak calling by Sparse Enrichment
887 Analysis for CUT&RUN chromatin profiling. Epigenetics Chromatin *12*, 42.
888 10.1186/s13072-019-0287-4.
889 62. Zhu, L.J. (2013). Integrative analysis of ChIP-chip and ChIP-seq dataset. Methods in
890 molecular biology (Clifton, N.J.) *1067*, 105-124. 10.1007/978-1-62703-607-8_8.
891 63. Team, B.C.M., B.P. (2019). TxDb.Drerio.UCSC.danRer11.refGene: Annotation package for
892 TxDb object(s).
893 64. Love, M.I., Huber, W., and Anders, S. (2014). Moderated estimation of fold change and
894 dispersion for RNA-seq data with DESeq2. Genome biology *15*, 550. 10.1186/s13059-
895 014-0550-8.
896 65. Wu, T., Hu, E., Xu, S., Chen, M., Guo, P., Dai, Z., Feng, T., Zhou, L., Tang, W., Zhan, L., et al.
897 (2021). clusterProfiler 4.0: A universal enrichment tool for interpreting omics data.
898 Innovation (Camb) *2*, 100141. 10.1016/j.xinn.2021.100141.
899 66. Ramirez, F., Ryan, D.P., Gruning, B., Bhardwaj, V., Kilpert, F., Richter, A.S., Heyne, S., Dundar,
900 F., and Manke, T. (2016). deepTools2: a next generation web server for deep-sequencing
901 data analysis. Nucleic acids research *44*, W160-165. 10.1093/nar/gkw257.
902 67. Stuart, T., Srivastava, A., Madad, S., Lareau, C.A., and Satija, R. (2021). Single-cell chromatin
903 state analysis with Signac. Nature methods *18*, 1333-1341. 10.1038/s41592-021-01282-
904 5.
905 68. Butler, A., Hoffman, P., Smibert, P., Papalexi, E., and Satija, R. (2018). Integrating single-
906 cell transcriptomic data across different conditions, technologies, and species. Nature
907 biotechnology *36*, 411-420. 10.1038/nbt.4096.
908 69. Sagerström, C.G., Gammill, L.S., Veale, R., and Sive, H. (2005). Specification of the
909 enveloping layer and lack of autoneuralization in zebrafish embryonic explants.
910 Developmental dynamics : an official publication of the American Association of
911 Anatomists *232*, 85-97. 10.1002/dvdy.20198.
912 70. Jin, S., Guerrero-Juarez, C.F., Zhang, L., Chang, I., Ramos, R., Kuan, C.H., Myung, P., Plikus,
913 M.V., and Nie, Q. (2021). Inference and analysis of cell-cell communication using CellChat.
914 Nature communications *12*, 1088. 10.1038/s41467-021-21246-9.
915 71. Farrell, J.A., Wang, Y., Riesenfeld, S.J., Shekhar, K., Regev, A., and Schier, A.F. (2018). Single-
916 cell reconstruction of developmental trajectories during zebrafish embryogenesis. Science
917 (New York, N.Y.) *360*. 10.1126/science.aar3131.
918 72. Cao, J., Spielmann, M., Qiu, X., Huang, X., Ibrahim, D.M., Hill, A.J., Zhang, F., Mundlos, S.,
919 Christiansen, L., Steemers, F.J., et al. (2019). The single-cell transcriptional landscape of
920 mammalian organogenesis. Nature *566*, 496-502. 10.1038/s41586-019-0969-x.
921 73. Nowotschin, S., Setty, M., Kuo, Y.Y., Liu, V., Garg, V., Sharma, R., Simon, C.S., Saiz, N.,
922 Gardner, R., Boutet, S.C., et al. (2019). The emergent landscape of the mouse gut
923 endoderm at single-cell resolution. Nature *569*, 361-367. 10.1038/s41586-019-1127-1.

74. Pijuan-Sala, B., Griffiths, J.A., Guibentif, C., Hiscock, T.W., Jawaid, W., Calero-Nieto, F.J., Mulas, C., Ibarra-Soria, X., Tyser, R.C.V., Ho, D.L.L., et al. (2019). A single-cell molecular map of mouse gastrulation and early organogenesis. Nature *566*, 490-495. 10.1038/s41586-019-0933-9.

75. Sagerstrom, C.G., Gammill, L.S., Veale, R., and Sive, H. (2005). Specification of the enveloping layer and lack of autoneuralization in zebrafish embryonic explants. Developmental dynamics : an official publication of the American Association of Anatomists *232*, 85-97. 10.1002/dvdy.20198.

Figures:

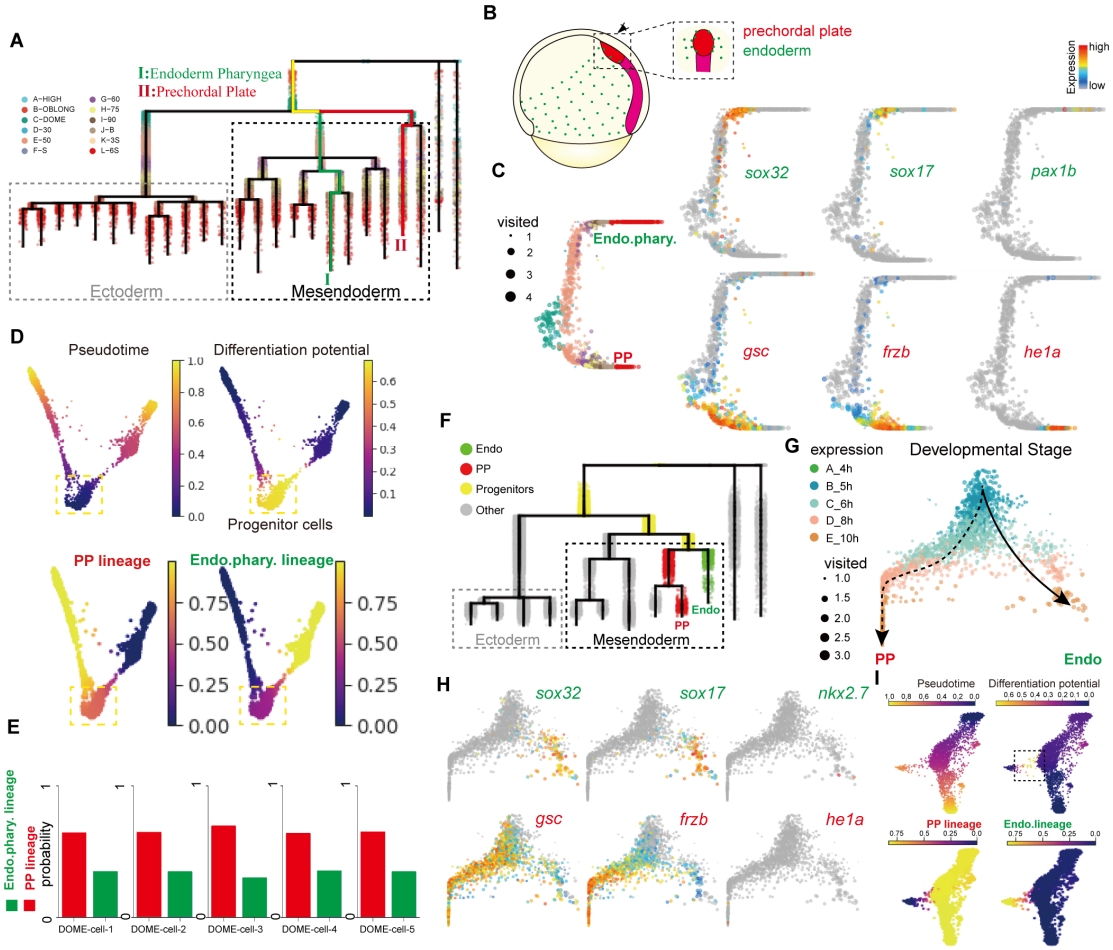

Figure 1. Single-cell trajectory analysis for studying PP and anterior Endo specification. (A) URD differentiation tree of zebrafish embryos from blastula stage to somitogenesis stage[74]. Cells are colored according to developmental stages. Gray dotted frame indicates the ectoderm lineages and black dotted frame indicates the mesendoderm lineages. Green line shows the

942 pharyngeal endoderm lineage (anterior endoderm, roman number I), red line shows the
943 prechordal plate lineage (roman number II) and yellow line indicates their progenitors. (B)
944 Simplified schematic showing the patterns of endoderm and axial mesoderm of zebrafish
945 embryos at 75% epiboly. Dotted frame indicates the enlarged view of dorsal anterior region,
946 showing that anterior Endo sporadically locates near PP. (C) URD branchpoint plots of the PP
947 and anterior Endo development from scRNA-seq data of zebrafish embryos[74], showing
948 pseudotime (x-axis) and random walk visitation preference from pharyngeal endoderm to
949 prechordal plate domains (y-axis). Cells are colored by developmental stages (left) and
950 expression of Endo markers (*sox32*, *sox17* and *pax1b*; right top) and PP markers (*gsc*, *frzb* and
951 *he1a*; right bottom). (D) Force-directed layout of PP and anterior Endo cells of zebrafish
952 embryos from blastula stage to somitogenesis stage. Cells are colored by Palantir[27] pseudotime
953 (top left), differentiation potential (top right) and branch probabilities of PP (bottom left) and
954 anterior Endo (bottom right). (E) Branch probabilities of five cells randomly selected from
955 progenitor cells. Bars are colored by cell types. (F) URD differentiation tree of Nodal explants
956 from blastula stage to the end of gastrulation. Gray dotted frame indicates the ectoderm lineages
957 and black dotted frame indicates the mesendoderm lineages. The green, red and yellow dots
958 indicate the Endo cells (anterior Endo), PP cells and the progenitor cells respectively, and the
959 gray dots indicate other cells. (G-H) URD branchpoint plots of the PP and Endo development
960 from scRNA-seq data of Nodal explants showing pseudotime (y-axis) and random walk
961 visitation preference from PP to Endo domains (x-axis). Cells are colored by developmental
962 stages (G) and expression of Endo markers (*sox32*, *sox17* and *nkx2.7*; top) and PP markers (*gsc*,
963 *frzb* and *he1a*; bottom) (H). (I) Force-directed layout of PP and anterior Endo cells of Nodal
964 explants from blastula stage to the end of gastrulation. Cells are colored by the levels of
965 Palantir[27] pseudotime (top left), differentiation potential (top right) and branch probabilities of
966 PP (bottom left) and anterior Endo (bottom right).
967

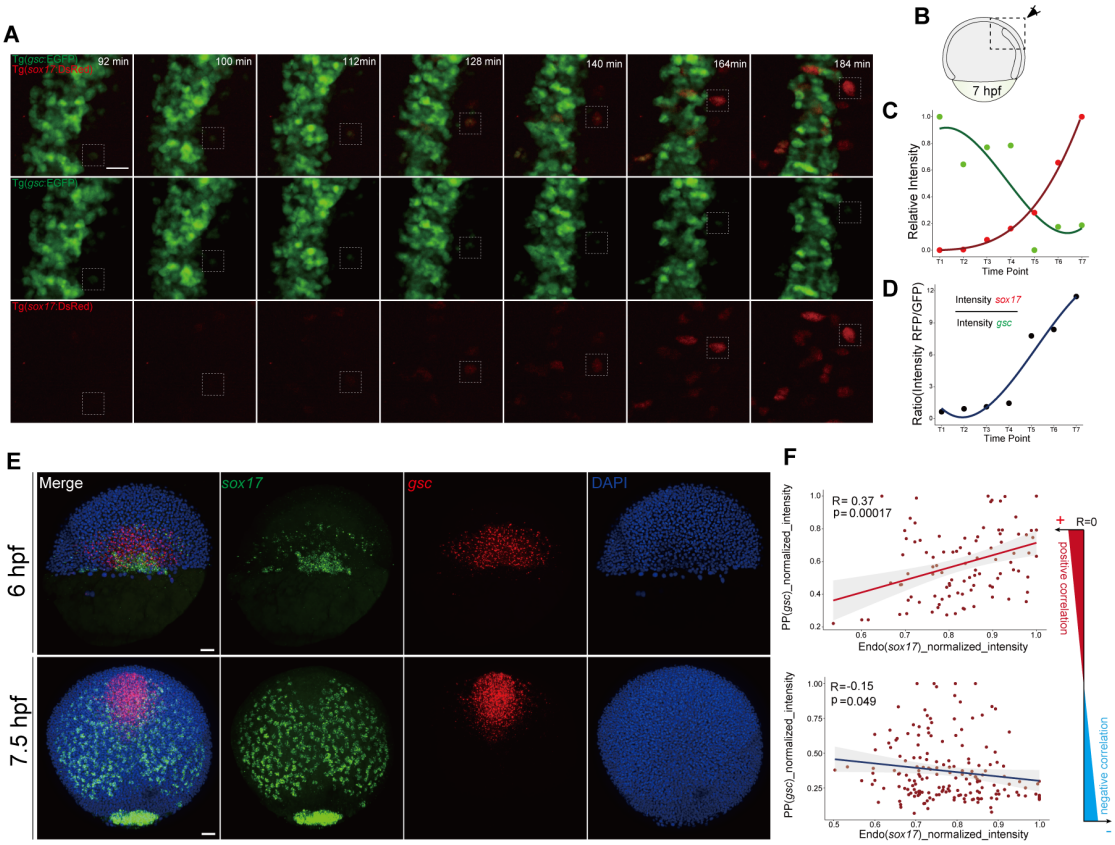

Figure 2. Live imaging analyses for Tg(*gsc*:EGFP;*sox17*:DsRed) embryos. (A) Time series of 3D reconstruction of a representative Tg(*gsc*:EGFP;*sox17*:DsRed) embryo. (B) Schematic diagram indicating the focused region in the Tg(*gsc*:EGFP;*sox17*:DsRed) embryo. (C and D) Temporal profiles of *sox17* (RFP) & *gsc* (GFP) (C) and the ratio between RFP intensity and GFP intensity (D) in the highlighted cell from (A). (E) Double-color RNA-fluorescence *in situ* hybridization (FISH) of *sox17* and *gsc* in wild-type embryos at 6 hpf (top) and 7.5 hpf (bottom). (N >= 30, n = 5/5, 6 hpf; N >= 30, n = 5/5, 7.5 hpf; N: embryos were used in the experiment; n: embryos were imaged, expression observed/total imaged) (F) Scatter plots and inferred linear regression comparing the relative intensities of *sox17* and *gsc* in wild-type embryos at 6 hpf (top) and 7.5 hpf (bottom). Each FISH experiment was performed for at least 3 independent replicates (technical replicates). Scale bar: 30 μm (A) and 50 μm (E).

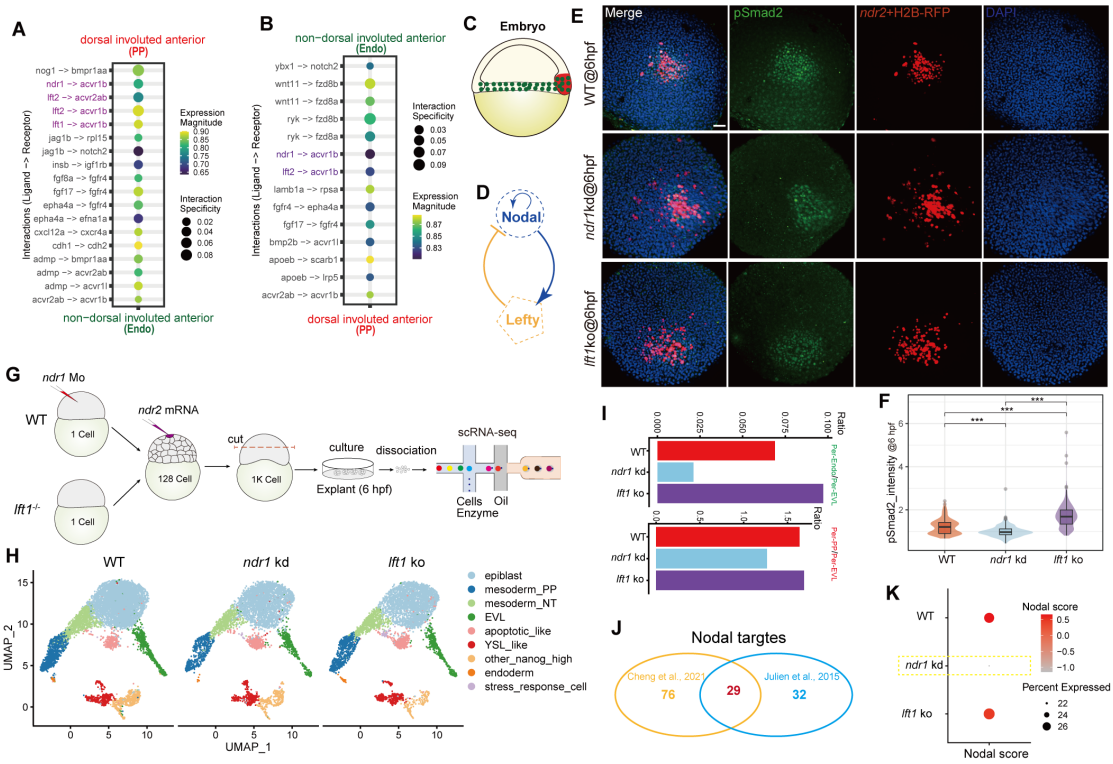

Figure 3 Nodal-Lefty regulatory loops are involved in cell fate separation between anterior Endo and PP. (A and B) Dot plots visualizing ligand-receptor interactions between PP and Endo. The interactions from PP (ligand) to Endo (receptor) and from Endo (ligand) to PP (receptor) are plotted respectively in A and B. (C) Schematic diagram illustrating PP (red) and Endo (green) in zebrafish embryos at 6 hpf. (D) Simplified schematic showing the interaction network between Nodal and Lefty. (E) 3D reconstruction of representative confocal-scanned images showing pSmad2 levels in zebrafish embryonic animal pole stimulated by Nodal injection at 128-cell stage (WT, N >= 10, n = 3/4; *ndr1*kd, N >= 10, n = 3/4; *lft1*ko, N >= 10, n = 4/4; N: embryos were used in the experiment; n: embryos were imaged, observed/total imaged). (F) Comparisons of pSmad2 levels in wild-type embryos, *lft1* mutants and *ndr1* morphants at 6 hpf (quantified from E). Statistical differences between two samples were evaluated by Student's t-test. *indicates P-value < 0.05, **indicates P-value < 0.01 and ***indicates P-value < 0.001. (G) Schematic diagram showing the experimental workflow of single-cell RNA sequencing of Nodal explants constructed from *lft1* mutants and *ndr1* morphants at 6 hpf. (H) Overall UMAP plot of integrated single-cell datasets of Nodal explants generated from wild-type embryos (left), *ndr1* morphants (middle) and *lft1* mutants (right). (I) Histograms showing the ratios of the cell proportions of endoderm against EVL (top) and

prechordal plate (bottom) against EVL. Per indicates percentage. As EVL cells can be specified spontaneously and are Nodal-independent[75], here the proportions of prechordal plate and endoderm were adjusted by using the proportions of EVL cells as an internal control. (J) Venn plot showing the selection of Nodal direct target genes used for defining Nodal score (**see Methods**). (K) Dot plot visualizing Nodal score in wild-type, *ndr1*-morphant and *lft1*-mutant Nodal explants. Dot size indicates the percentage of cells within the cell group; the color indicates the average Nodal score levels. Scale bar: 50 μm (E).

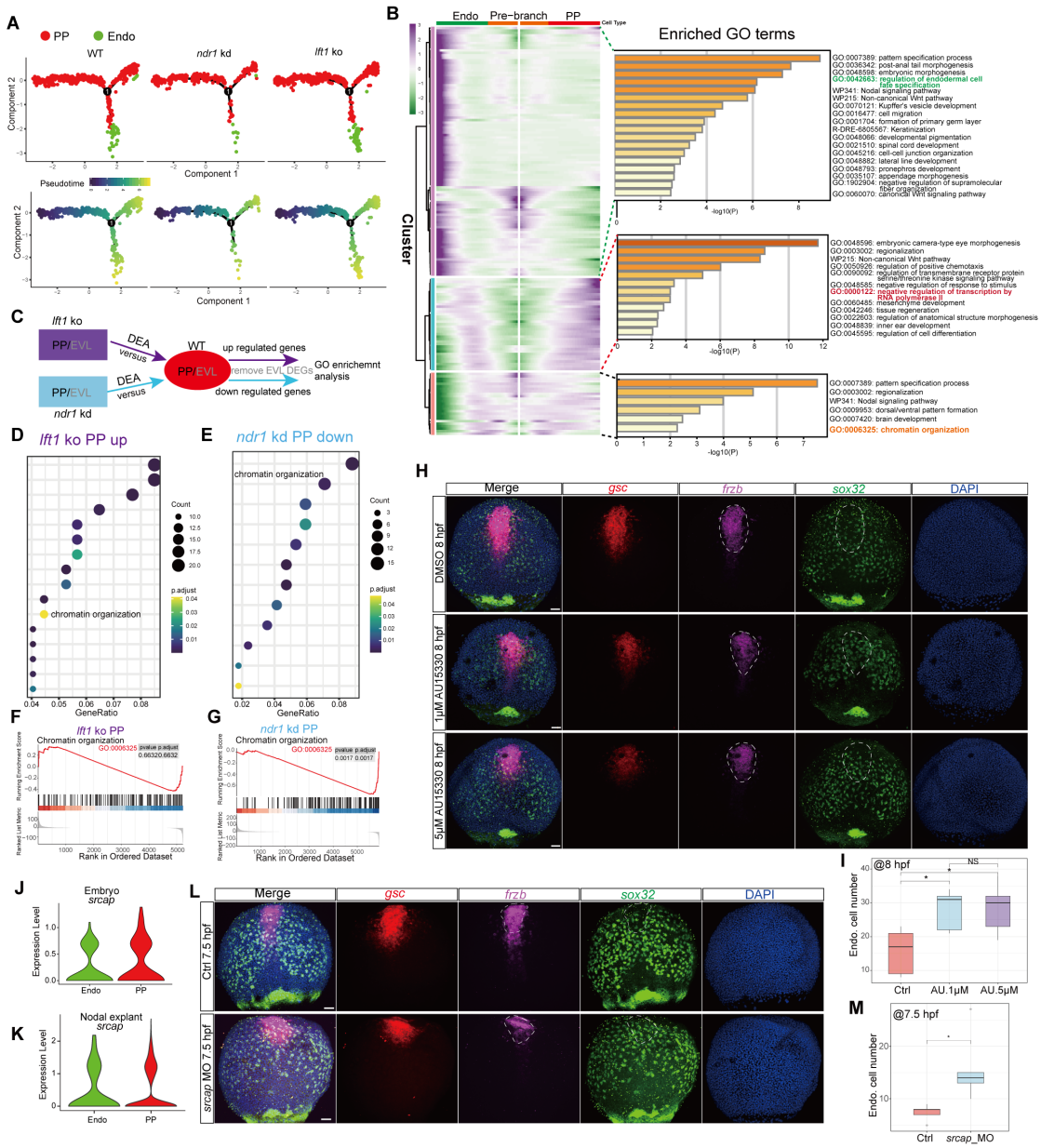

Figure 4. Single-cell trajectory tree analyses of PP and anterior Endo reveal that chromatin organization is involved in the separation of these two lineages. (A) Pseudotime trajectory analysis of PP and anterior Endo using integrated single-cell datasets of wild-type (left), *ndr1*-morphant (middle) and *lft1*-mutant (right) Nodal explants. Cells are colored by cell types (top) and pseudotime levels (bottom). (B) Heatmaps representing clusters of genes that co-vary along the pseudotime during the separation of PP and anterior Endo from common progenitors. Top GO terms enriched by the genes in each cluster are listed with their corresponding adjusted P-values. Representative GO terms of each cluster are highlighted in different colors. (C) Diagram of gene set selection for GO analysis. As a control of batch effects,

EVL differentially expressed (DE) genes are removed from mesoderm PP DE genes. (D and E) GO enrichment analysis of mesoderm PP up-regulated genes in *lft1* mutants (D) and down-regulated genes in *ndr1* morphants (E). Redundancy of enriched GO terms are removed, and each GO term contains at least 10 transcripts. Note that only the top 16 enriched GO terms identified in *lft1* mutant are plotted for a visualization purpose. (F and G) GSEA of "chromatin organization" term on PP cells from *lft1* mutants (F) and *ndr1* morphants (G) respectively. P-adjust indicates Benjamini-Hochberg adjusted p-value. (H-M) SWI/SNF complexes involved in regulating cell fate separation between the PP and anterior Endo. (H) HCR co-staining of *gsc*, *frzb* and *sox32* in wild-type embryos (top, N >= 40, n = 5/5, N: embryos were used in the experiment, n: embryos were imaged, expression observed/total imaged), as well as those treated with 1 μM (middle, N >= 40, n = 4/5, N: embryos were used in the experiment, n: embryos were imaged, expression observed/total imaged) and 5 μM (bottom, n = 5/6, expression observed/total imaged) AU15330. Regions framed by dotted white lines were used to quantify the cell number of anterior Endo. (I) Box plot showing the cell numbers of anterior Endo in (H). (J and K) Volinplot indicating the expression levels of *srcap* in PP and Endo cells within both embryos (J) and Nodal explants (K). (L) HCR co-staining of *gsc*, *frzb* and *sox32* in wild-type embryos and embryos with *srcap* knockdown. Embryos at 7.5 hpf (Ctrl, N >= 30, n = 6/6; *srcap* MO, N >= 30, n = 4/5; N: embryos were used in the experiment; n: embryos were imaged, expression observed/total imaged) were evaluated. (M) Box plot showing the cell numbers of anterior Endo in (L). Statistical differences between two samples were evaluated by Student's t-test (I and M). *indicates P-value < 0.05; NS indicates P-value >=0.05. Each HCR experiment was performed for at least 3 independent replicates (technical replicates). Scale bar: 50 μm (H and L).

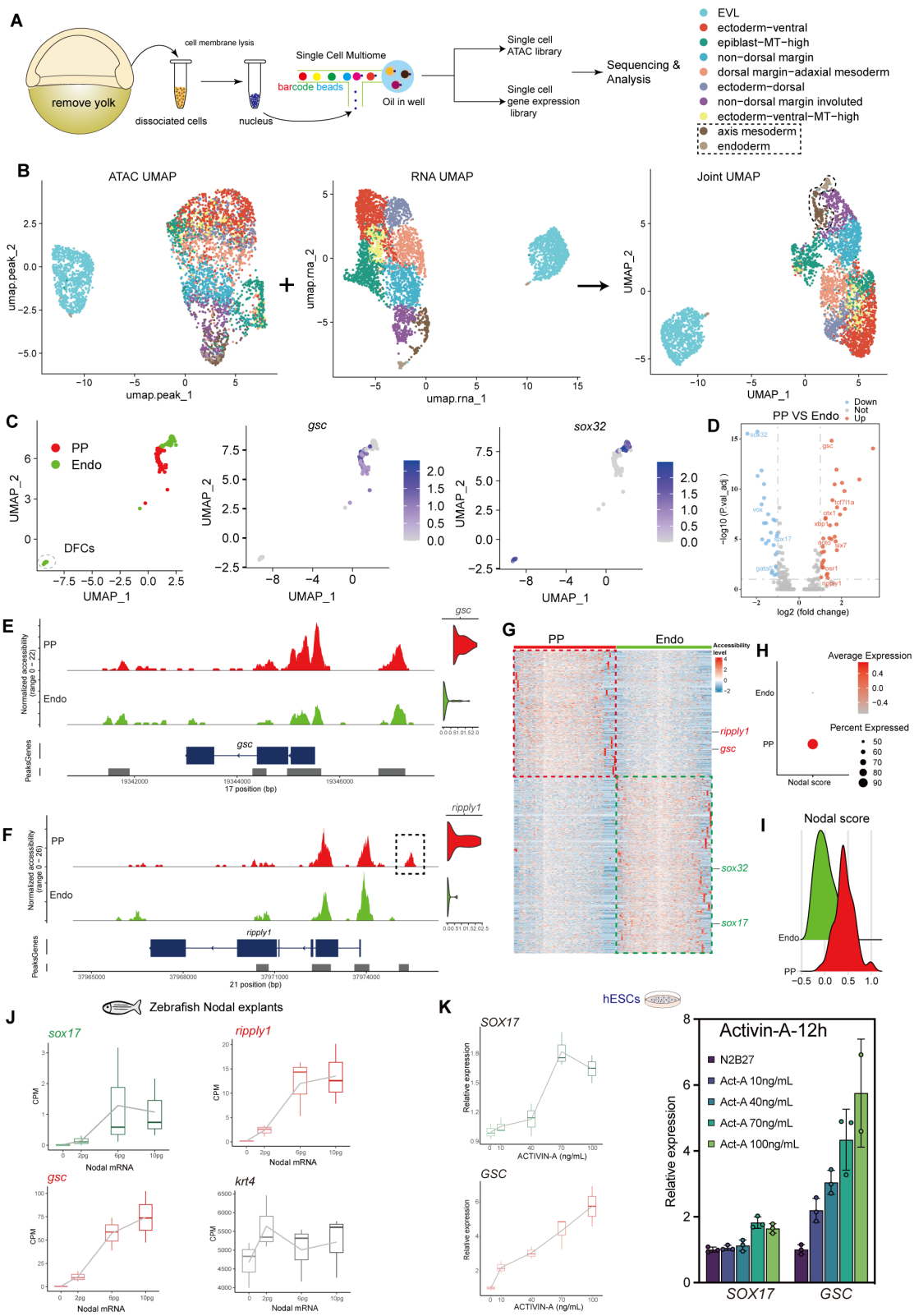

Figure 5. Investigating the mechanisms of PP and Endo separation through integrative single-cell RNA-seq and ATAC-seq analysis. (A) Schematic diagram showing the experimental workflow of single-cell multi-omics of 6 hpf zebrafish embryos. (B) UMAPs

based on scATAC-Seq (left), scRNA-Seq (middle) and co-embedding scRNA-seq and scATAC-seq (right) datasets. Cells are colored by different cell types. (C) UMAP plot of the PP and Endo cells. Cells are colored by cell types (left) and the expression of *gsc* (middle) and *sox32* (right). (D) Volcano plot showing the differentially expressed genes in PP and Endo based on RNA levels of single-cell multi-omics datasets. (E-F) Track plot showing chromatin accessibility of each cell type on the gene locus of *gsc* (E) and *ripply1* (F). (G) Heatmap showing the chromatin accessibility level of genes with differential chromatin accessibility in PP and Endo. Red and green box indicates genes with higher chromatin accessbility levels in PP and Endo cells respectively. (H and I) Dot plot (H) and ridge plot (I) showing the level of Nodal score in PP and Endo. (J) Box plots showing the expression profiles of *sox17* (Endo), *gsc* (PP), *ripply1* (PP) and *krt4* (EVL) in our previous bulk RNA-seq datasets of Nodal explants. (K) Box plots (left) and bar plot (right) showing the expression levels of *SOX17* and *GSC* in the human embryonic stem cells (hESCs) treated with different dosages of Activin protein (**see Methods**). The values were calculated as the mean ± SEM (K).

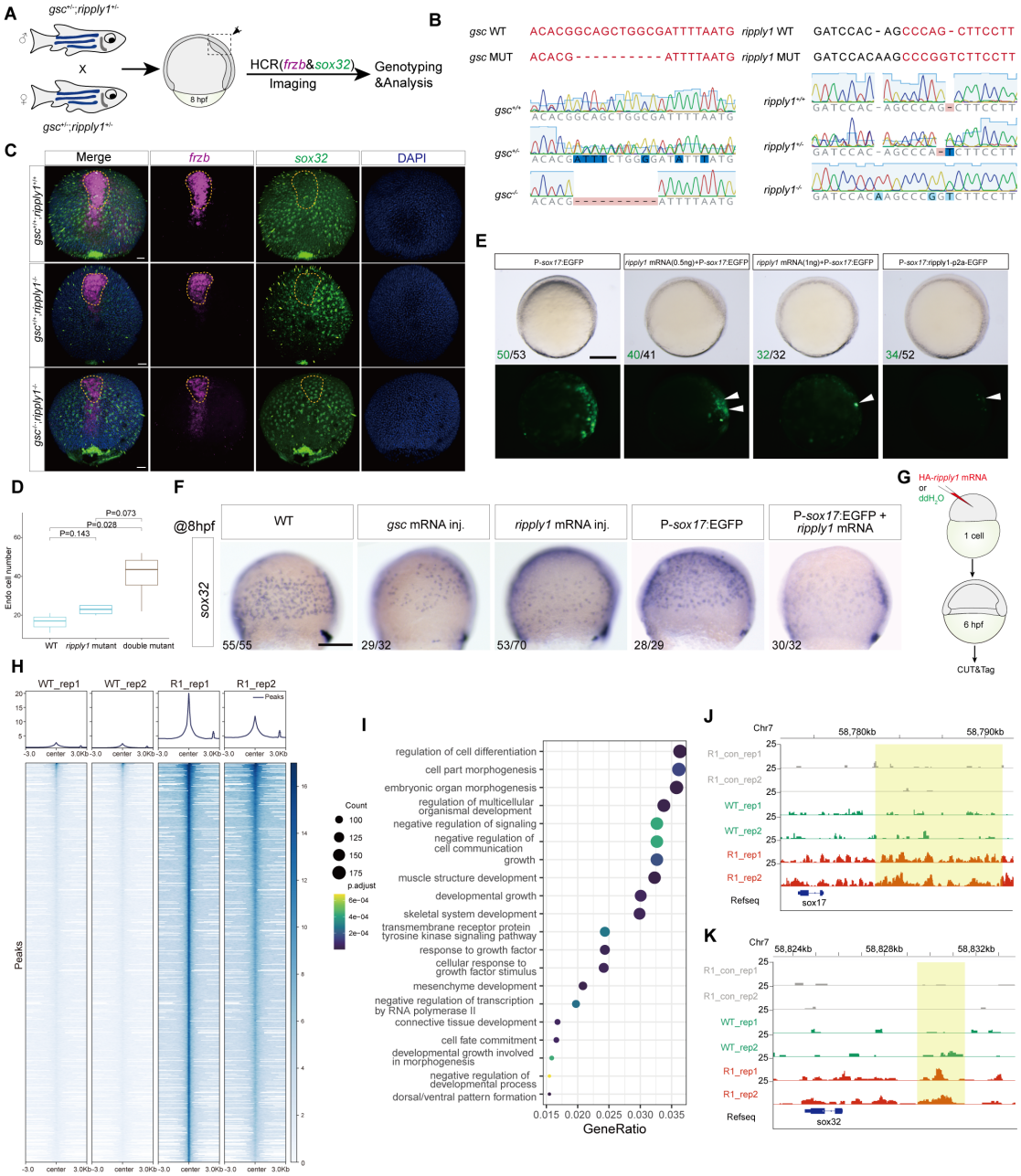

Figure 6. Exploring the mechanisms underlying the role of Ripply1 in the regulation of cell fate separation between PP and anterior Endo. (A) Schematic diagram illustrating the workflow for investigating the role of *gsc* and *ripply1* in mesendoderm cell fate separation through loss-of-function studies. (B) Schematic presentation of *gsc* and *ripply1* mutations and the sequencing results of each genotype. The mutations are a 10-bp deletion and a 1-bp insertion in *gsc* and *ripply1* coding sequences respectively. Texts in red indicate coding sequences. Sanger sequencing results display at the bottom, showcasing wild-type (top), heterozygous mutant (middle) and homozygous mutant (bottom) embryos of *gsc* and *ripply1* mutations. (C) HCR co-staining of *sox32* and *frzb* in the embryos of Tg(*gsc*$^{+/+}$;*ripply1*$^{+/+}$) (WT),

Tg(*gsc*$^{+/+}$;*ripply1*$^{-/-}$) (*ripply1* mutant) and Tg(*gsc*$^{-/-}$;*ripply1*$^{-/-}$) (double mutant) at 8 hpf (Here embryos of three different genotypes are shown. Other genetypes are shown in Figure S10A.) [Tg(*gsc*$^{+/+}$;*ripply1*$^{+/+}$), n = 4/5; Tg(*gsc*$^{+/+}$;*ripply1*$^{-/-}$), n = 4/6; Tg(*gsc*$^{-/-}$;*ripply1*$^{-/-}$), n = 5/5; expression observed/total imaged]. (D) Box plot showing the quantification of the numbers of anterior Endo cells identified in (C). (E and F) Assessing the role of *ripply1* in anterior Endo specification. EGFP driven by *sox17* promotor (E) and WISH of *sox32* (F) are used to indicate the Endo cells. Embryos with *gsc* overexpression are used as a positive control. The statistics of observed/total sampled embryos were shown in bottom left of the panels (E and F). (G) Schematic diagram showing the strategy of conducting CUT&Tag experiment for *ripply1*. (H) Metaplots and heatmaps for CUT&Tag signals over R1_rep1 binding peaks (n=72,683) in wild-type and HA-*ripply1*-injected embryos. Two replicates were performed. (I) Dot plot showing the enriched GO terms using the genes that annotated from the differentially enriched peaks. (J and K) Screenshot of R1_con (technical control, without primary antibody, **see Methods**), WT (ddH_2O-injected) and R1 (HA-*ripply1*-injected) CUT&Tag peaks around *sox17* (J) and *sox32* (K) loci. Each HCR and ISH experiment was performed for at least 3 independent replicates (technical replicates). Statistical differences between two samples were evaluated by Student's t-test (D). Scale bar: 50 μm (C) and 200 μm (E and F).

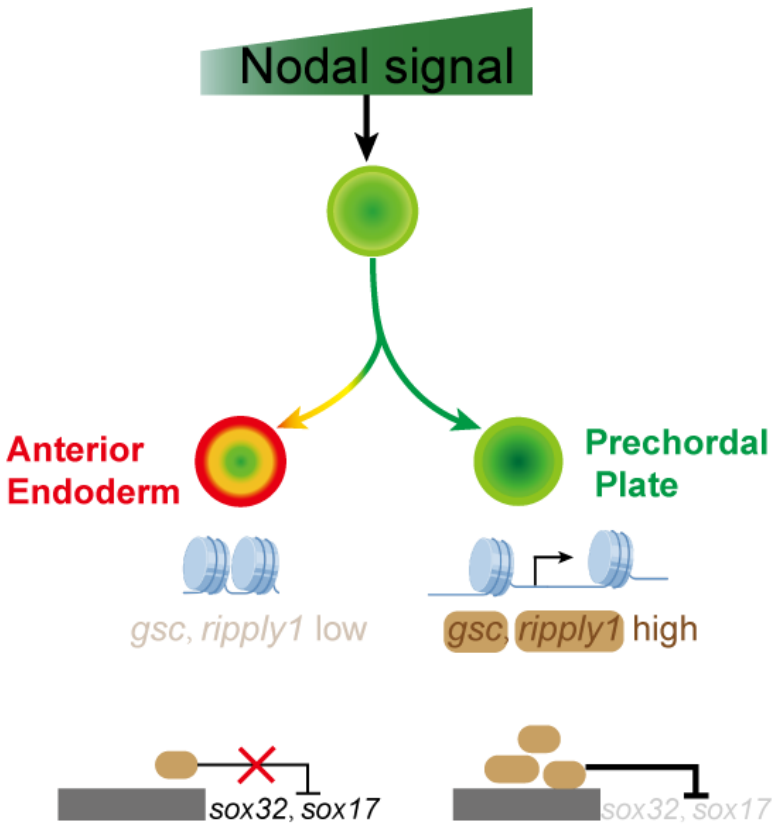

Figure 7. Model underlying the separation of PP and anterior Endo. An outline depicts PP and anterior Endo specification. Nodal signaling drives a differential chromatin states between PP and anterior Endo through epigenetic regulators. And then, key transcriptional factors, such as *gsc* and *ripply1*, are differentially expressed in these two lineages and suppress anterior Endo specification by directly binding to the *cis*-elements of *sox17* and *sox32*.

Acknowledgments:

We would like to thank Dr. Alex Schier for his kind gift of the *lft1* mutant. We thank Dr. Ming Shao from Shandong University for his kind gift of the *ripply1* mutant. We thank Dr. Peng Xia from Zhejiang University for his kind gift of the Tg(*gsc*:EGFP) embryos. We also thank Dr. Nai-He Jing at University of Chinese Academy of Sciences, Dr. Jun Ma, Dr. Xiao-hang Yang, Dr. Min-Xin Guan, Dr. Feng He and the members of Laboratory of Development and Organogenesis (LDO) at Zhejiang University for helpful suggestions and discussions. We thank Mr. Guang-Xu Zhang from Biostar Technology for the technical help on constructing 10x single-cell multi-omics sequencing library. We thank Shuang-Shuang Liu from the Imaging Platform and Ying-Niang Li from the zebrafish core facility at Zhejiang University School of

Medicine for their technical support. This work was supported by grants from the Chinese National Key Research and Development Project (2022YFA1103100, 2019YFA0802402) and the National Scientific Foundation of China (32050109, 32300688, 32300677).

Conflict of Interest:

The authors declare no competing interests.

Author Contributions

PFX, TC and HQL conceived and designed the research; TC, XL, YD, YMT, YYX, CYC, CL, YFL, YH, DHZ, XX, XXF, ZXJ, JYL and JM performed research; TC and YD analyzed the single-cell RNA-seq and single-cell multi-omics data; YD performed the CUT&Tag experiment and analyzed the data; TC, YD, HQL and PFX wrote the manuscript; all authors reviewed and approved the manuscript. PFX and HQL supervised this study. Fundings for the study were provided by PFX, TC and YD.